IMPLEMENTATION OF AN ACOUSTO-OPTIC METHOD FOR DETERMINING PHOTOELASTIC TENSOR ELEMENTS IN GLASS

by

Christopher Sutherland

Submitted in partial fulfillment of the requirements
for the degree of Master of Science

at

Dalhousie University
Halifax, Nova Scotia
December 2021

Table of Contents

List of Tables

List of Figures

Abstract

Glass is an amorphous solid and in a stress-free environment exhibits isotropic optical properties. When such a material is placed under stress the optical properties become anisotropic. Glass can be characterized by its stress-optic response which describes how the optical properties will change when it is subject to stress.

The mechanical properties were measured for three Ohara glass samples as well as for fused quartz which was used to test the accuracy of the Dixon-Cohen method used in this thesis for the measurement of the individual photoelastic tensor elements.

The stress-optic response of all glass samples was investigated using the Sénarmont compensator method and the Dixon-Cohen method. The Dixon-Cohen method is shown to be an accurate method for the determination of the individual photoelastic tensor elements of glass samples.

List of Abbreviations

AR anti-reflective

EBPVD Electron-beam physical vapour deposition

KK Kramers-Kronig

LCVR liquid crystal variable retarder

SBS Stimulated Brillouin Scattering

Chapter 1

Introduction

The scientific interest in the properties of glass goes back over 400 years, however, the investigation of the photoelastic properties has only been investigated over the past few decades. The importance of understanding these properties plays a key role in fiber optic cable design.

Fiber optic cables are widely used in telecommunication and therefore the understanding of the limitations of optical fibers is important. Finding an accurate way to measure the individual photoelastic tensor elements will allow for the understanding of new ways to design fiber optic cables with longer transmission ranges.

The objective of this thesis is to investigate the accuracy of the Dixon-Cohen method for the measurement of the photoelastic properties of various glasses. Using the Sénarmont compensator and the Dixon-Cohen acousto-optic setup the stress-optic coefficients can be measured and compared.

This thesis is comprised of six chapters. Chapter 2 describes what glass is and theories that attempt to correlate the mechanical properties of glass to the photoelastic properties of interest. The theory behind the various measurement techniques used throughout this thesis is also described to provide the reader with a better understanding of the results obtained.

Chapter 3 goes into detail about the operation of each technique used to measure various properties of the glass samples. The processing of the glass samples is outlined in detail as well as each of the optical setups used in this thesis.

Chapter 4 presents the results obtained for the mechanical properties of the

glasses. The refractive index measurements using the Abbe refractometer as well as the spectral ellipsometer are also provided. Finally, the data for the Sénarmont compensator and the acousto-optic data from the Dixon-Cohen setup are presented.

Chapter 5 provides a discussion of the results obtained and possible reasons for the disagreement of the measured properties compared to previously reported data on the glass samples.

Finally, Chapter 6 provides concluding remarks on the results obtained in this thesis and outlines future improvements that could be done to achieve more accurate results.

Chapter 2

Background

Glass, unlike crystals, have no long-range atomic order. These materials are known as amorphous solids and have isotropic optical properties under a stress-free environment. These materials have many applications being used industrially as glass windows, and personally for optometry and for glass screens of smartphones. They are also extremely important in lens design for microscopes and telescopes. One of the more leading fields of glass science is the usage of optical fibers in communication networks. Understanding the properties of glass is important to the future of communication, as well as many other fields.

2.1 Glass Structure

This thesis focuses on a method to measure the photoelastic properties of glass that will provide the groundwork necessary to correlate the individual photoelastic tensor elements to the structure of the glass system. In this section, the general structure of oxide glasses will be introduced and further explained by the random network theory hypothesis.

2.1.1 The Definition of Glass

The structure of glass is different from the crystalline structure because there is no long-range order due to the lack of a periodic structure. Glass is formed by heating certain compounds to liquid form, at which point they are super-cooled, preventing the atoms from returning to their relaxed crystalline lattice sites.

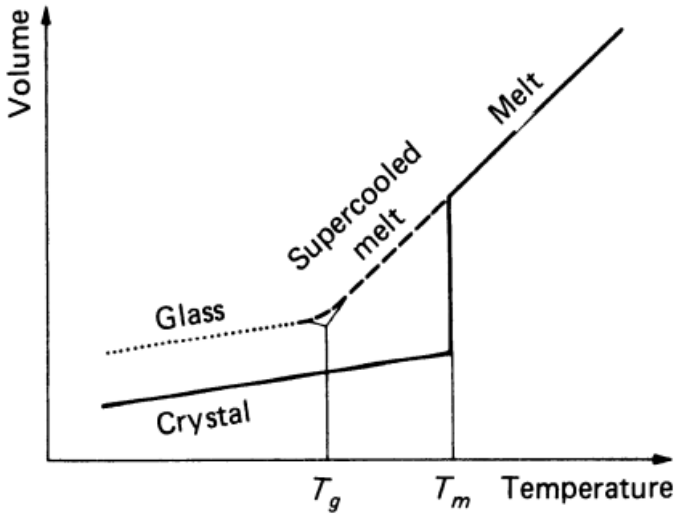

Figure 2.1: Volume dependence on formation of glass compared with crystal structure with temperature [1].

Figure 2.1 shows that if a liquid cools slowly a crystal is formed, and at the melting temperature, T_m, a large volume change occurs (this process is reversible). However, if the liquid is super-cooled the atoms become frozen in place and cannot return to the relaxed crystalline lattice locations, and glass is formed. The glass transition temperature, T_g, describes the temperature range in which glass will form. In an oxide glass, the structure tends to have a small variation in bond length and a large variation in bond angles compared to the crystalline equivalent.

2.1.2 Random Network Theory

The definition of glass is disputed amongst the scientific community. A widely accepted theory for the formation of oxide glasses was presented by Zachariasen in 1932 [4]. First, he stated that an oxide glass of the composition A_mO_n the oxygen atoms can be bonded to no more than two A atoms. He also proposed that A atoms are only surrounded by a small amount of oxygen atoms and the oxygen polyhedra do not share edges or faces, only corners with each other shown in Figure 2.2 **b**. Finally, he suggested that for each polyhedron at least three corners must be shared. This

theory sufficiently describes the structure of glasses such as SiO_2, however fails to explain the structure of other types of glasses such as metallic glasses. Figure 2.2

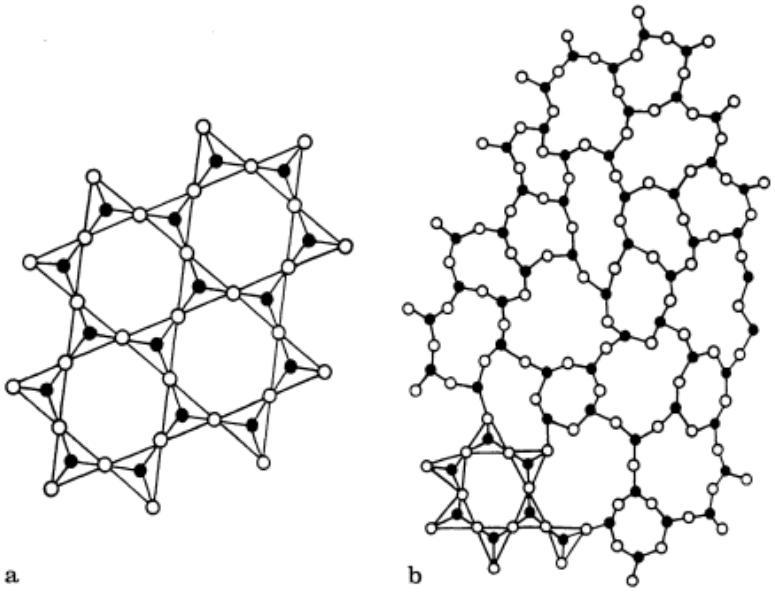

Figure 2.2: **a.** Crystalline structure of SiO_2 where black dots are Si atoms and white dots are O atoms. **b.** Glass structure of SiO_2 [2]. This is a schematic representation of an ordered crystal (left) and a disordered glass (right). For a disorder glass the bond lengths are largely preserved, however, the bond angles vary largely.

a. shows the crystalline form of SiO_2 where the bond lengths and bond angles are all equivalents. In Figure 2.2 **b.** the glass form of SiO_2 is shown, where the bond lengths vary by small amounts and the bond angles vary quite significantly. In this representation the oxygen bonds between silicon atoms are known as bridging oxygen bonds. Oxygen bonds that are only bonded to one Si atom with one free end are known as non-bridging oxygen.

2.1.3 The Glass Network

The Zachariasen network theory is valid for low-order glass systems composed of simple oxide compounds such as SiO_2, B_2O_2, P_2O_5, and GeO_2 [2]. These compounds will form a glass by themselves with a similar structure to that shown in Figure 2.2

b. They are known as glass network formers because they can form a glass network without the addition of other compounds.

Other compounds can be added to these networks and are known as network modifiers. Examples of glass network modifiers are Na_2O or CaO. When these compounds are introduced to the glass network some of the oxygen bonds between the anions in the glass are broken, forming non-bridging oxygen bonds shown in Figure 2.3. The

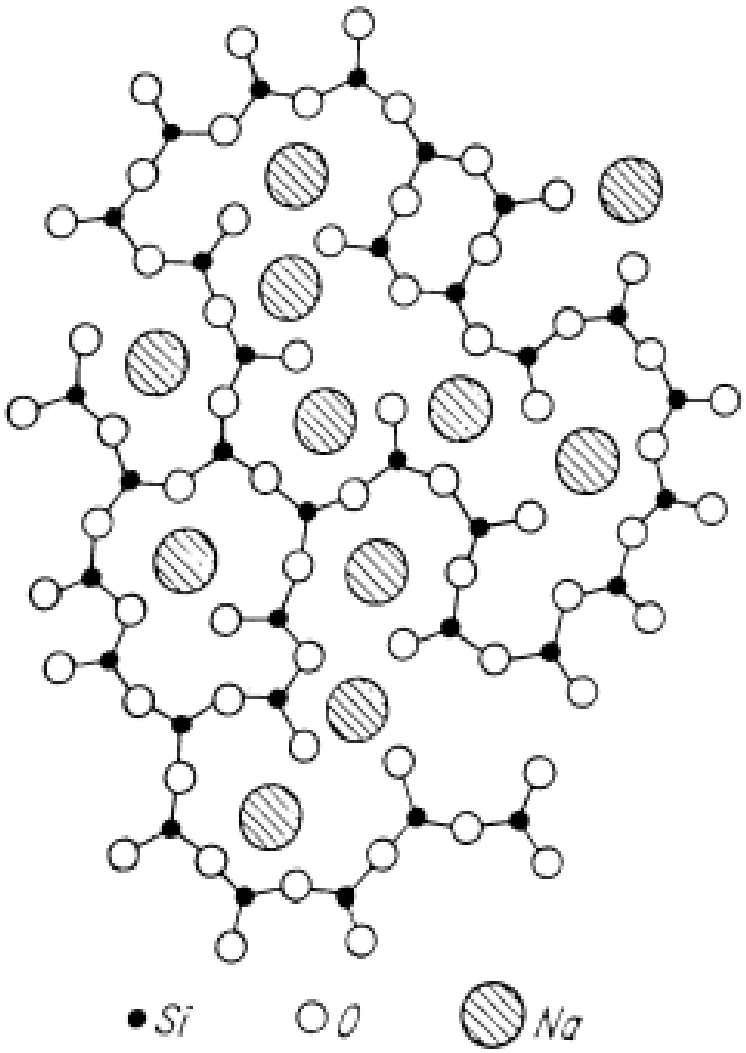

Figure 2.3: The addition of Na_2O to an SiO_2 glass creating non-bridging oxygen bonds [2].

addition of these compounds modifies the properties of the glass, such as the melting

temperature, mechanical properties, and optical properties. The melting temperature of SiO_2 is 1700 °C, but with the addition of 33 mol % Na_2O the melting temperature is reduced significantly to less than 800 °C [5].

Another classification of compounds are known as intermediates. These compounds can act as the glass modifier or as the glass former. An example of such a compound is PbO which can change the optical properties of the glass such as the index of refraction, photoelastic coefficients, density, and more [6].

2.2 Interaction of Light with Glass

2.2.1 Birefringence

When glass is stressed the optical properties are no longer isotropic. A stress-induced glass exhibits birefringent effects, changing the index of refraction along the extraordinary (stress direction) n_e and ordinary axes n_o. When a stress is introduced the change in the refractive indices results in birefringence,

$$b = n_e - n_o. \tag{2.1}$$

This induced birefringence is shown in Figure 2.4 where the change in the index of refraction parallel to the stress is called the extraordinary axis and the change perpendicular is called the ordinary axis. The birefringence is proportional to the applied stress, provided the stress is within the elastic limit of the glass, by

$$b = C\sigma \tag{2.2}$$

C is known as the stress-optic coefficient and is used to characterize a glasses birefringent response to an applied stress. The stress-induced birefringence in glass can also be described using the piezo-optic tensor π_{ijrs}, or the elasto-optic tensor, p_{ijkl}.

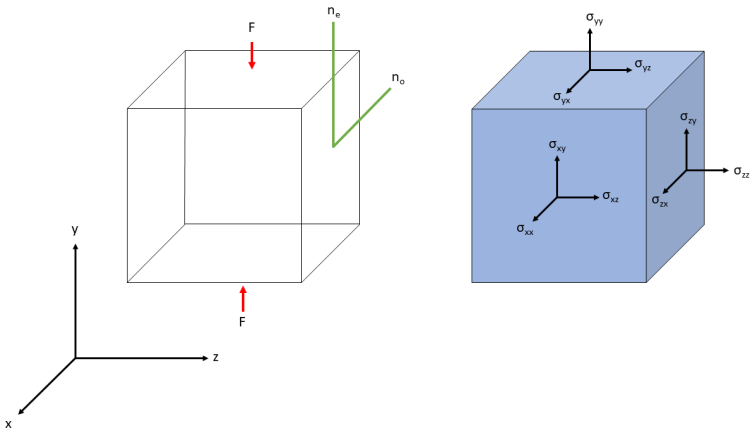

Figure 2.4: Uniaxial stress-induced birefringence resulting in the change of the indices of refraction along the extraordinary (n_e) and ordinary (n_o) axes. This results in an induced birefringence $b = n_e - n_o$.

These tensors relate the applied stress or strain to the change in the inverse dielectric constant:

$$\Delta B_{ij} = \pi_{ijrs}\sigma_{rs} = p_{ijkl}s_{kl} \tag{2.3}$$

where $B_{ij} = (1/n^2)_{ij} = (1/\epsilon)_{ij}$ is the inverse dielectric tensor, σ_{rs} is the stress tensor, and s_{kl} is the strain tensor [7, 8]. A force that is exerted on a face of the cube will cause a stress along the y-axis shown in Figure 2.4, as well as stresses orthogonal to it. This can be expressed by the stress tensor σ_{rs}. The elasto-optic tensor can be written in terms of the piezo-optic tensor by $p_{ijkl} = \pi_{ijrs}C_{rskl}$, where C_{rskl} is the compliance tensor. Voigt notation is used due to the symmetry of the tensor where the following simplification can be made:

$$11 \rightarrow 1,\ 22 \rightarrow 2,\ 33 \rightarrow 3,\ 23 \rightarrow 4,\ 13 \rightarrow 5,\ 12 \rightarrow 6$$

Due to glass being isotropic, only two of the three piezo-optic and elasto-optic tensor elements are independent, and are related by

$$\begin{aligned} 2p_{44} &= p_{11} - p_{12} \\ 2\pi_{44} &= \pi_{11} - \pi_{12} \end{aligned} \tag{2.4}$$

Equation 2.3 can be solved for a uniaxial stress assuming the change in refractive index is small ($n_e \approx n_o \approx n$). This results in Equation 2.3 becoming

$$\Delta B_e = \frac{1}{n_e^2} - \frac{1}{n^2} = \frac{n^2 - n_e^2}{n^2 n_e^2} = \frac{(n_e + n)(n - n_e)}{n^2 n_e^2} = \frac{(n - n_e)(2n)}{n^4} = \pi_{33}\sigma_3 = \pi_{11}\sigma_3, \tag{2.5}$$

which can be written as

$$(n - n_e) = \frac{n^3}{2}\pi_{11}\sigma_3. \tag{2.6}$$

Similarly we can show for the ordinary axis that

$$\Delta B_o = \frac{1}{n_o^2} - \frac{1}{n^2} = \frac{n^2 - n_o^2}{n_o^2 n^2} = \frac{(n_o + n)(n - n_o)}{n_o^2 n^2} = \frac{(n - n_o)(2n)}{n^4} = \pi_{13}\sigma_3 = \pi_{12}\sigma_3, \tag{2.7}$$

which can be written as

$$(n - n_o) = \frac{n^3}{2}\pi_{12}\sigma_3. \tag{2.8}$$

This can be related to birefringence, b, by relating the stress-optic coefficient to the piezo-optical coefficients. Subtracting Equation 2.6 from Equation 2.8 gives

$$b = (n_e - n_o) = -\frac{n^3}{2}(\pi_{11} - \pi_{12})\sigma_3 = C\sigma_3. \tag{2.9}$$

C is often used to describe the behaviour of a glass under stress and can be written in terms of the shear piezo-optic tensor element as

$$C = -n^3\pi_{44}. \tag{2.10}$$

As well, this can be written in terms of the shear elasto-optic tensor element as

$$C = -\frac{n^3}{2G}p_{44} \tag{2.11}$$

where $G = C_{44}$ is the shear modulus of the glass.

The composition of a glass determines whether it will have a positive, negative, or zero stress-optic coefficient. Studies have shown that the addition of heavy elements such as lead, bismuth, tin, and antimony can lower the stress-optic coefficient and can in some cases introduce a zero or negative stress-optic response [7, 9]. The fundamental goal of many glass scientists since the 1900's when Pockel's first studied photoelasticity has been to relate the stress-optic response of glass to its structure [10].

2.2.2 Theories of Photoelasticity: Elasto-Optic Coefficients

Several theories have attempted to relate the elasto-optic tensor elements of crystals and amorphous materials to the material properties and composition. Many of these theories and models have predicted the relationship of photoelasticity to the dielectric tensor, polarizability density tensor, and chemical bonding in the material. In order to understand the connection between photoelasticity and the structure two straightforward models will be described.

2.2.2.1 Clausius-Mossotti Model

To understand the relationship between photoelasticity and these material properties a simple model will first be considered. The Clausius-Mossotti model is considered to be the first step to understanding the full relationship between these properties. This model shows the relationship between the dielectric constant (or the refractive index) and the polarizability of the material. It works well for homogeneous isotropic materials and can be applied to less ideal liquids and solids.

Consider an electric field, $\boldsymbol{E}$, which is related to the total polarization, $\boldsymbol{P}$, by

$$\boldsymbol{P} = (\epsilon - 1)\epsilon_o \boldsymbol{E} \tag{2.12}$$

where ϵ is the dielectric constant of the material, and ϵ_o (8.85 x $10^{-12}C^2N^{-1}m^{-2}$) is the dielectric constant of free space.

If one considers N_L dipoles per unit volume then the total polarization can be written as

$$\boldsymbol{P} = N_L\alpha\boldsymbol{E}' \tag{2.13}$$

where α is defined as the mean polarizability of each dipole and $\boldsymbol{E}'$ is the local electric field applied on the average dipole. For glass and other dense dielectric materials the local field can be described by the macroscopic field and the Lorentz field which are dependent on the polarization

$$\boldsymbol{E}' = \boldsymbol{E} - \frac{1}{3\epsilon_o}\boldsymbol{P} \tag{2.14}$$

The Clausius-Mossotti equation can be found by combining Equation 2.12, Equation 2.13, and Equation 2.14 and setting $4\pi\epsilon_o = 1$ giving

$$\frac{\epsilon - 1}{\epsilon + 2} = \frac{4\pi N_L\alpha}{3} = \frac{4\pi N\alpha}{3V_m} = \frac{4\pi N\rho\alpha}{3M} \tag{2.15}$$

where N is Avogadro's number, ρ is the density, V_m is the molar volume and M is the molar mass of the material. The Lorentz-Lorenz equation can be found by substituting $\epsilon = n^2$ giving

$$\frac{4\pi N_L\alpha}{3} = \frac{(n^2-1)}{(n^2+2)}V_m = R_m, \tag{2.16}$$

where R_m is referred to as the molar refractivity.

If a perfect, isotropic, homogeneous material is considered where α has no density dependence ($d\alpha/d\rho = 0$), the dielectric response of the material can be related to the

elasto-optic tensor elements by

$$3\rho\frac{d\epsilon}{d\rho} = \epsilon^2(p_{11} + 2p_{12}) = (\epsilon - 1)(\epsilon + 2) \tag{2.17}$$

This model is considered one of the simpler representation of photoelasticity, however, it is a good starting point for further models to be built on.

2.2.2.2 Mueller's Model

In 1935 Mueller considered two additional effects to the Lorentz-Lorenz equation. Firstly, he considered the lattice effect which describes the change in Lorentz-Lorenz forces in a solid. Secondly, he considered the atomic effect which describes changes in the mean polarizabilities due to strain deformations in the material. Equation 2.14 describes the local electric field on an average dipole in the material. For multi-atom systems we can write the Lorentz-Lorenz equation as

$$\frac{n^2 - 1}{n^2 + 2} = \rho \sum \frac{4\pi N \alpha_i}{3M_i}, \tag{2.18}$$

where the summation is over atoms of type i. This equation is valid for an unperturbed homogeneous isotropic material. If a strain in the z-direction is introduced the Lorentz-Lorenz forces will become dependent on the local electric field. In this case the strain ellipsoid would be 1:1:1+z, and the local electric field components would be

$$\begin{aligned} E_x^{'} &= E_x + \frac{P_x}{\epsilon_o}\left(\frac{1}{3} + \frac{2}{15}z\right), \\ E_y^{'} &= E_y + \frac{P_y}{\epsilon_o}\left(\frac{1}{3} + \frac{2}{15}z\right), \\ E_z^{'} &= E_z + \frac{P_z}{\epsilon_o}\left(\frac{1}{3} + \frac{4}{15}z\right). \end{aligned} \tag{2.19}$$

By substituting Equation 2.12 and Equation 2.13 into Equation 2.19 the following indices of refraction are obtained:

$$\begin{aligned} n_x^2 - 1 &= \sum \frac{4\pi N \rho \alpha_i}{M_i} \left[1 + \left(\frac{1}{3} + \frac{2}{15} z \right) (n_x^2 - 1) \right], \\ n_y^2 - 1 &= \sum \frac{4\pi N \rho \alpha_i}{M_i} \left[1 + \left(\frac{1}{3} + \frac{2}{15} z \right) (n_y^2 - 1) \right], \\ n_z^2 - 1 &= \sum \frac{4\pi N \rho \alpha_i}{M_i} \left[1 + \left(\frac{1}{3} - \frac{4}{15} z \right) (n_z^2 - 1) \right]. \end{aligned} \tag{2.20}$$

The elasto-optic tensor elements can be found by differentiating the terms in Equation 2.20 about $z = 0$ and considering α_i to be constant with respect to z. This results in

$$\begin{aligned} p_{12} &= \frac{1}{3} \frac{(\epsilon - 1)(\epsilon - 2)}{\epsilon^2} - \frac{2}{15} \frac{(\epsilon - 1)^2}{\epsilon^2} \\ p_{11} &= \frac{1}{3} \frac{(\epsilon - 1)(\epsilon - 2)}{\epsilon^2} + \frac{4}{15} \frac{(\epsilon - 1)^2}{\epsilon^2} \end{aligned} \tag{2.21}$$

Mueller attributed the first terms in both of the above equations to be a result of the change in density of a material under a strained state [11]. He states that because this is typically a large positive number, it explains why p_{11} and p_{12} always have positive values. The second term in the above equation is responsible for the birefringence observed due to the anisotropy in the Lorentz-Lorenz force. The shear elasto-optic coefficient is then found to be $2p_{44} = 6(n^2 - 1)^2/15n^4$ and provides the correct order of magnitude, however, fails to provide the correct sign compared to experimental data. The failure to predict the correct sign of the stress-optic coefficient led to the consideration of a change in polarizability.

In order to predict the positive and negative stress-optic response of glass Mueller

considered the change in the polarizability of the atoms. He assumed that the polarizability would behave linearly due to the linearity of the photoelastic effect giving

$$\begin{aligned} \alpha_z &= \alpha(1+\lambda_1 z), \\ \alpha_{x.y} &= \alpha(1+\lambda_2 z). \end{aligned} \tag{2.22}$$

Taking this into consideration introduces a third term into the elasto-optic tensor elements making them

$$\begin{aligned} p_{12} &= \frac{1}{3}\frac{(\epsilon-1)(\epsilon-2)}{\epsilon^2} - \frac{2}{15}\frac{(\epsilon-1)^2}{\epsilon^2} - \frac{L_2}{3}\frac{(\epsilon-1)(\epsilon+2)}{\epsilon^2}, \\ p_{11} &= \frac{1}{3}\frac{(\epsilon-1)(\epsilon-2)}{\epsilon^2} + \frac{4}{15}\frac{(\epsilon-1)^2}{\epsilon^2} - \frac{L_1}{3}\frac{(\epsilon-1)(\epsilon+2)}{\epsilon^2}, \\ 2p_{44} = p_{11} - p_{12} &= \frac{(L_2-L_1)}{3}\frac{(\epsilon-1)(\epsilon+2)}{\epsilon^2} + \frac{6}{15}\frac{(\epsilon-1)^2}{\epsilon^2}, \end{aligned} \tag{2.23}$$

where L_1 and L_2 represent the optical deformabilites of the atoms' polarizability. It can be defined as $L_{1,2} = \sum(\lambda_{1,2}N\alpha/M)_i / \sum(N\alpha/M)_i$. The presence of this new term in the above equation explains how glasses can have positive, negative or zero birefringence based on the values of L_1 and L_2.

Mueller states that in heavier glasses the term $\left(\frac{6}{15}\frac{(\epsilon-1)^2}{\epsilon^2}\right)$ will be larger due to larger refractive indices. The stress-optic coefficient C is related to the elasto-optic tensor element p_{44} and can be used to relate the structure, arrangement of molecules, and deformations in glass due to stress. However, because L_1 and L_2 need to be determined experimentally this theory is limited.

2.2.2.3 Theories of the Dispersion of the Photoelastic Tensor Elements

Most theories for the dispersion of the photoelastic tensor elements pertain to crystalline materials, however, an understanding of these theories may provide insight into properties that could lead to a connection between the dispersive nature in amorphous solids.

Wemple and DiDomenico considered how strain on a crystal would change the energy band structure. This was then used to model the dispersion of the elasto-optic tensor in crystalline materials. The strain-induced changes to the energy band structure were determined by approximating the band structure with a simple oscillator model [12]. The imaginary part of the dielectric response, $\epsilon_{2,ij}$, can be determined from the one-electron wave function. The real part can be determined using the Kramers-Kronig (KK) integral in the region of transparency by

$$\epsilon_{1,ij} - 1 = \frac{2}{\pi} \int_{\omega_g}^{\infty} \frac{\omega' \epsilon_{2,ij}(\omega')}{\omega'^2 - \omega^2} d\omega' \tag{2.24}$$

where ω_g represents the absorption threshold frequency. When a strain is applied the wave functions and energy bands will change. This results in a change to the real part of the dielectric function resulting in

$$\Delta\epsilon_{1,ij}(\omega) = \frac{2}{\pi} \int_{\omega'_g}^{\infty} \frac{\omega' \Delta\epsilon_{2,ij}(\omega')}{\omega'^2 - \omega^2} d\omega' \tag{2.25}$$

where $\Delta\omega_g$ is the shift in the absorption threshold due to the induced-strain, and $\omega'_g = \omega_g + \Delta\omega_g$. The elasto-optic tensor elements can be related to this when there is an induced-strain x by

$$\Delta\epsilon_{1,ij}(\omega) = -\sum_{k,l} \epsilon_{1,ik} \Delta(1/\epsilon_1)_{kl} \epsilon_{1,lj} = -\sum_{k,l,m,n} \epsilon_{1,ik} \epsilon_{1,lj} p_{klmn} x_{mn}. \tag{2.26}$$

In order to determine the imaginary part of the dielectric function, $\Delta\epsilon_{2,ij}$, the authors used the simple oscillator approximation. Using the Sellmeier expression the contribution of the band structure to the dielectric constant can be modeled for ionic and covalent crystals

$$\epsilon_1(\lambda) - 1 = S_0(\lambda_0)^2 \left[1 - \left(\frac{\lambda_0}{\lambda} \right)^2 \right]^{-1}. \tag{2.27}$$

Here S_0 is the oscillator strength, λ is the wavelength of light, and λ_0 is the oscillator position parameter. The oscillator strength is related to the interband strength ($\mathcal{F} = (hc/e)^2 S_0$), and the oscillator position parameter is related to the interband energy ($\mathcal{E}_0 = hc/e\lambda_0$). Equation 2.27 is considered to be a long-wavelength approximation to the KK integral which leads to

$$\begin{aligned}(\mathcal{E}_0)^2 &= \left(\frac{\hbar}{e}\right)^2 \int_{w_g}^{\infty} \frac{\epsilon_2}{\omega} d\omega \Big/ \int_{w_g}^{\infty} \frac{\epsilon_2}{\omega^3} d\omega, \\ \mathcal{F} &= \frac{2}{\pi}\left(\frac{\hbar}{e}\right)^2 \left(\int_{w_g}^{\infty} \frac{\epsilon_2}{\omega} d\omega\right)^2 \Big/ \int_{w_g}^{\infty} \frac{\epsilon_2}{\omega^3} d\omega.\end{aligned} \tag{2.28}$$

When there is an induced strain there will be a change in the oscillator position ($\Delta\mathcal{E}_0$) and the oscillator strength ($\Delta\mathcal{F}$). These can be calculated using Equation 2.28. Using the Sellmeier expression, the change in the real part of the dielectric constant can be calculated under an induced-strain by

$$\begin{aligned}\frac{\Delta\epsilon_1}{(\epsilon_1 - 1)} &= -2\left(\frac{\Delta\mathcal{E}_0}{\mathcal{E}_d}\right)\left(1 + \mathcal{K}_{ij}\left[1 - \left(\frac{\lambda_0}{\lambda}\right)^2\right]\right), \\ \mathcal{K}_{ij} &= -\frac{1}{2}\left(\frac{\Delta\mathcal{F}/\mathcal{F}}{\Delta\mathcal{E}_0/\mathcal{E}_0}\right).\end{aligned} \tag{2.29}$$

Here $\mathcal{E}_d = \mathcal{F}/\mathcal{E}_0 = (hc/e)S_0\lambda_0$ is the dispersion energy. Introducing a deformation potential parameter $\mathcal{D}_{ij}$ that relates the strain component x_{ij} to the oscillator shift $\Delta\mathcal{E}_0$ by the following

$$\Delta\mathcal{E}_0 = \sum_{i,j} \mathcal{D}_{ij} x_{ij} \tag{2.30}$$

Under the assumption that $\mathcal{E}_d$, $\mathcal{E}_0$, and ϵ_1 are approximately isotropic, the elasto-optic

coefficients can be described by

$$\frac{p_{ij}}{(1-1/n^2)^2} = \frac{2}{\mathcal{E}_d}\mathcal{D}_{ij}\left(1+\mathcal{K}_{ij}\left[1-\left(\frac{\lambda_0}{\lambda}\right)^2\right]\right). \tag{2.31}$$

In the case of Equation 2.31 the values of $\mathcal{D}_{ij}$ and $\mathcal{K}_{ij}$ can be measured experimentally and p_{ij} can be calculated. The dispersive nature of p_{ij} depends on the value of $\mathcal{K}_{ij}$ and will determine if it is positive or negative. The dispersion energy was previously described by Wemple and DiDomenico empirically [13]:

$$\mathcal{E}_d = \beta N_c Z_a N_e, \tag{2.32}$$

where β experimentally takes the value of $\beta_i = 0.26$ eV for ionic compounds and $\beta_c = 0.39$ eV for covalent compounds. N_c represents the cation coordination number, Z_a is the formal anion valency, and N_e is the effective number of valance electrons per anion.

Wemple and DiDomenico showed that Equation 2.31 is an effective two-parameter fit for the elasto-optic dispersion of crystalline materials. Although this fit resulted in reasonable values it provided no correlation between the crystal composition and the properties of the crystals.

Cardona *et al.* considered relating the photoelastic properties of amorphous solids and crystalline materials to the electronic band structure [14]. Cardona considered how the electronic contributions would affect the piezo-optic tensor elements. The dispersion of the piezo-optic tensor elements shows strong dispersion near their absorption edge. This tends to be stronger at direct edges compared to indirect gaps.

Cardona looked at the band structure of Ge crystal under strain to investigate the change in the optical properties. The focus was on the contribution of E_0 (transparent region) and E_1 (outside the transparent region) transitions to the change in piezo-optic

tensor π_{ijkl}. The piezo-optic tensor can be calculated from the analytical expression of the dielectric constant which is in terms of these energy gaps.

When the Ge crystal is under a hydrostatic stress (X_H) the direct gap energy E_0 and the spin-orbit splitting component $E_0 + \Delta_0$ are affected and can be represented by dE_0/dX_H resulting in the hydrostatic constant

$$(\pi_{11} + 2\pi_{12})_{E_0, E+\Delta_0} = \frac{1}{2\omega_0}\frac{d\omega_0}{dX_H}P^{-1}\left(G^{(3)}(x) + 3F^{(3)}(x) + \frac{1}{2}G^{(3)}(x') + \frac{3}{2}F^{(3)}(x')\right), \tag{2.33}$$

where

$$\begin{aligned} G^{(3)}(x) &= \frac{1}{x^2}[2 - (1+x)^{-1/2} - (1-x)^{-1/2}], \\ F^{(3)}(x) &= \frac{1}{x^2}[2 - (1+x)^{1/2} - (1-x)^{1/2}]. \end{aligned} \tag{2.34}$$

Here $x = \omega/\omega_0$, $x' = \omega/(\omega_0 + \Delta_0)$, and where $P = 2\pi/a_0$ is the interband matrix element of linear momentum and a_0 is the lattice constant.

There are two things that affect the shear terms of π_{ijkl} arising from E_0 in the Ge crystal. The first effect comes from the splitting $\delta\omega_0$ of the top valance band Γ_8 caused by the shear stress, and the second arises from the coupling of Γ_8 with the spin-orbit split state Γ_7. This leads to the hydrostatic constants

$$\begin{aligned} \pi_{11} - \pi_{12} &= \frac{3}{4}(S_{11} - S_{12})\frac{b}{\omega_0}P^{-1}\left(-G^{(3)}(x) + \frac{4\omega_0}{\Delta_0}\left[F^{(3)}(x) - \left(\frac{\omega_0}{\omega_0 - \Delta_0}\right)^{3/2}F^{(3)}(x')\right]\right), \\ \pi_{44} &= \frac{3}{4}S_{44}\frac{d}{2\sqrt{3}\omega_0}P^{-1}\left(-G^{(3)}(x) + \frac{4\omega_0}{\Delta_0}\left[F^{(3)}(x) - \left(\frac{\omega_0}{\omega_0 - \Delta_0}\right)^{3/2}F^{(3)}(x')\right]\right), \end{aligned} \tag{2.35}$$

where b and d are typically negative values and are known as shear deformation potentials. $G^{(3)}$ describes the effect of the band splitting, and $F^{(3)}$ represents the band

coupling. For the crystals considered in this study the values of P^{-1}, S_{ij}, b and d are approximately equal requiring the addition of a constant term for the experimental measurements to match the theory. The positive constant term dominates at low frequencies, however with a changing wavelength, the negative dispersive term will dominate and result in an isotropic point for particular materials. In the case of ω_0 being small the shear effects due to the E_0 edge will overcome the constant term and will result in no isotropic point.

Cardona states that the elasto-optic tensor elements p_{ij} can be compared to the experimentally determined values if the deformation potentials (b and d), ω_0, and Δ_0 are all known. This possesses a problem for glass materials due to the fact that the electronic band structure of glass is difficult to obtain.

Kucharczyk took a similar approach as Wemple and DiDomenico and consider a single oscillator in order to show the wavelength dependence of the elasto-optic tensor [15]. From a bond polarizability approach the shear component of the elasto-optic tensor is

$$p_{44} = \frac{8}{n^4 a^3}(\beta^T - \beta^L), \tag{2.36}$$

where n is the refractive index, a is the lattice constant, and $\beta^{T,L}$ is the transverse and longitudinal part of the bond polarizability tensor. β^T and β^L were fit for alkali halides using the single oscillator formula for λ in the UV-vis range with

$$\beta^{T,L} = \frac{A^{T,L}\lambda^2}{\lambda^2 - (\lambda_0^{T,L})^2} \tag{2.37}$$

A limiting factor to this theory is the need to understand the dependence of β on the wavelength, particularly how the parameter A changes with wavelength. This is necessary in order to describe the relationship between p_{44} and λ.

All of these theories have limitations in describing the dispersive nature of p_{ij},

however it provides a good understanding of particular properties such as the refractive index, electronic band structure and bond polarizabilities that could help relate the chemical composition of a glass to the change in the elasto-optic tensor.

2.2.2.4 The Empirical Model of Photoelasticity

Guignard and Zwanziger developed an empirical model that predicts the sign of the stress-optic coefficient based on the bond length, d, and the coordination number, N_c [9]. This model predicts that if a glass has a low d/N_c it will have a positive stress-optic coefficient, and if it has a high d/N_c it will have a negative stress-optic coefficient. Glasses that have low coordination numbers allow for the distortion of the bonds along the bonding direction and orthogonal to it, whereas high coordination numbers prevent this from happening [9]. Therefore, high coordination number results in negative stress-optic coefficients and low coordination number results in positive stress-optic coefficients.

Guignard *et al.* [9] compiled a list of compounds with their d/N_c values and the sign of the stress-optic coefficient shown in Table 2.1.

Guingard states that in order to obtain a glass with a zero stress-optic coefficient the following must be true for a glass blend between one of the metallic components in Table 2.1 and a glass former

$$\sum_i x_i \left(\frac{d}{N_c}\right)_i \approx 0.5\text{Å}. \tag{2.38}$$

The summation in Equation 2.38 is over the compounds the glass is comprised of, x_i is the molar percentage of the ith compound, and (d/N_c) is the ratio listed in Table 2.1 for the particular compound. This model is useful in determining the sign of the stress-optic coefficient based on the compounds the glass is made of, however, it does not predict the magnitude of the stress-optic coefficient. As well, it does not

Table 2.1: The compound names are listed along with the anion-cation bond length d, the coordination number N_c, the ratio of the cation-anion bond with the coordination number d/N_c, and the sign of the stress-optic coefficient C. Values that were calculated from first principles are labeled 'calc' and those determined experimentally are labeled 'expt'.

Compound	d (Å)	N_c	d/N_c (Å)	sign of C	source
Tl_2O	2.517	3	0.84	−	expt [16]
Sb_2O_3	2.022	3	0.67	−	expt [9]
PbO	2.326	4	0.58	−	calc [9], expt [16]
SnO	2.224	4	0.56	−	calc, expt [9]
Bi_2O_3	2.198	4	0.55	−	expt [17]
TeO_2	2.0	4	0.50	+	calc [9]
ZnO	1.988	4	0.50	+	expt [18, 19, 20]
PbS	2.967	6	0.49	+	calc [9]
BaO	2.74	6	0.46	+	calc [9], expt [20]
B_2O_3	1.366	3	0.46	+	expt [18]
GeO_2	1.717	4	0.43	+	expt [21]
SiO_2	1.609	4	0.40	+	expt
P_2O_5	1.5	4	0.38	+	expt [22]
MgO	2.1085	6	0.35	+	calc [9], expt [20] [16]
SnO_2	2.055	6	0.34	+	calc [9]

predict the wavelength dependence of the stress-optic coefficient which is important when designing a zero-stress optic glass for a particular wavelength.

2.2.2.5 Other Works

Previous studies have been done that look at the elasto-optic tensor elements of various glass systems or industrially produced glasses. Early measurements of the individual elasto-optic tensor elements were done by Manenkov and Ritus who investigated the mechanical and photoelastic properties of laser glasses to determine their usefulness [23]. This was done by measuring the Brillouin spectra using a Fabry-Perot interferometer. This was later used by Heiman *et al.* to investigate the Brillouin spectra of 16 industrially provided optical glasses.

Benassi *et al.* furthered this by looking at the Brillouin spectra of several silicate glasses provided by Schott [24]. They reached the conclusion that for silicate glasses

that the bond polarizability model coupled with the dipole-induced-dipole model was useful in predicting the elasto-optic tensor elements, however further work was required.

Roselló *et al.* used whispering gallery mode resonances to investigate the dispersion of the elasto-optic coefficients in fibre optic cables under axial stress [25]. These measurements lead to the conclusion that silica shows a relatively flat dispersion response, however, due to large errors conclusive statements could not be made.

Galbraith *et al.* looked at several different families of glasses and how changes in the molar fraction of the composition related to changes in the elasto-optic coefficients [26]. She investigated barium borates, lead borates, barium phosphates, lead phosphates, and lead silicates using Brillouin spectroscopy. The author showed that an adapted bond polarizability model could be used to predict the sign and the values of the elasto-optic elements of unknown oxide glasses.

These models all suggest some form of predictability of the elasto-optic coefficients by a bond polarization model however more data is required in order to further understand the correlation between the glass structure and the photoelastic properties.

2.3 Acousto-Optics

Acousto-optics describe the interaction between electromagnetic waves and acoustic waves propagating through a material. This effect can occur in different mediums such as liquids, amorphous solids, or crystalline materials. When acoustic waves propagate through a material density fluctuations occur. These density fluctuations cause a change in refractive index, resulting in a localized change of the optical properties.

The field of acousto-optics is relatively new, beginning in the early 1900's when Brillouin first theorized that electromagnetic waves could interact with acoustic phonons propagating through a material. Debye and Sears as well as Lucas and Biquard later proved this experimentally [27].

The invention of the laser propelled the field of acousto-optics to what it is today [28]. Before the laser was invented various light sources were used such as mercury arc lamps. Mercury arc lamps produce light by discharging an electric arc through vaporized mercury. The light produced by these arc lamps is comprised of several different wavelengths in the ultra-violet range as well as the optical range. This is not ideal when trying to determine material properties that are wavelength dependent. The invention of the laser in 1960 provided a solution to this problem [28]. Lasers produce monochromatic coherent light, which is ideal when investigating material properties that are wavelength-dependent [29].

2.3.1 Acousto-Optics

Acousto-optic modulators are devices used to rapidly diffract light and typically operate under the Bragg condition. The Bragg condition usually refers to the atomic spacing between atoms in a crystal, however, in this circumstance it will be the wavelength of the acoustic beam which causes the density fluctuations in the material. The Bragg condition can be written as

$$\sin\theta_B = \frac{\lambda}{2\Lambda} \tag{2.39}$$

where θ_B is the Bragg angle, λ is the wavelength of the incident laser beam, and Λ is the wavelength of the acoustic wave.

At the Bragg angle, the incident light beam will be scattered at the same angle of the exiting surface. The intensity of the scattered beam can be expressed using the acousto-optic figure of merit

$$M = \frac{I}{P_a} = \frac{p_{ij} n^6}{\rho v^3} \tag{2.40}$$

where M is the acousto-optic figure of merit, I is the intensity of the diffracted beam,

P_a is the acoustic power density, p_{ij} is the individual photoelastic tensor element, n is the refractive index, ρ is the density, and v is the longitudinal speed of sound.

In the study of glass materials, the determination of the individual photoelastic tensor elements is of great interest. These properties have been studied dating back to the early 1900's [2]. The Dixon-Cohen method makes use of the ratio of the figure of merit for an unknown sample compared to that of a known reference sample such as fused quartz, which relates the diffracted intensities to the photoelastic coefficients [30]. The following equation shows the ratio of the figure of merits

$$\frac{M_{sample}}{M_{fusedquartz}} = \sqrt{\frac{I_4 I_5}{I_1 I_R}} = \frac{(p^2 n^6/\rho v^3)^{sample}}{(p^2 n^6/\rho v^3)^{fusedquartz}} \tag{2.41}$$

where I_i represents the measured intensity peaks labeled in Figure 3.7. I_1 is the scattered intensity through the reference from the initial outgoing acoustic wave in the reference sample. I_R is the scattered intensity through the reference from the acoustic wave after it has been transmitted into the sample, reflected off of the free end, and is re-transmitted back into the reference sample. I_4 is the scattered intensity through the sample from the initial acoustic wave that is transmitted into the sample from the reference sample. I_5 is the scattered intensity through the sample from the acoustic wave that has been transmitted into the sample and has reflected off the free end.

2.3.2 Stimulated Brillouin Scattering

In 1922 Léon Brillouin showed theoretically that optical photons could be scattered from thermally excited phonons in a material [31]. The scattering of optical photons by these thermally excited acoustic waves is a prominent property in materials and has gained much interest over the past century.

Stimulated Brillouin Scattering (SBS) limits the optical power that can be transmitted through an optical fiber over long distances and requires relay stations to amplify the signal [32]. Thus, investigating how to reduce the process of SBS is important in the field of optical fiber communication which is of major interest to industrial internet providers.

Brillouin scattering is a spontaneous event in which an incident photon is converted into a scattered photon and phonon in the material. The scattered photon undergoes a downshift in frequency and is known as a Stokes wave named after George Stokes who discovered this phenomenon in the 19^{th} century [33]. This process becomes stimulated in the backward direction as you increase the pump power of the input light into the fiber optic cable. This limits the distance in which an optical signal can be transmitted through an optical fiber, requiring relay stations to amplify the signal [32, 34].

The largest contribution to the SBS in optical fibers is due to electrostriction which causes a density change in insulating materials in the presence of a strong electric field. This causes the refractive-index to depend on the intensity of the incident light [35, 36]. The backscattered Stokes wave will interfere with the input light causing the formation of an acoustic wave due to electrostriction effect. The more intense the input light is the greater the amplitude of the acoustic wave becomes. As the acoustic wave propagates in the forward direction it acts as a Bragg grating, resulting in more light to be scattered in the backwards direction [33].

The following mathematical description of SBS closely follows the description given in reference [33]. As mentioned above, SBS is when an incident photon is scattered, resulting in the formation of a new photon and an acoustic phonon. From the perspective of quantum mechanics it can be thought of as the annihilation of the incident photon and the formation of a new scattered photon and phonon, where both energy and momentum are conserved. The relationship between the incident wave

frequency, also known as the pump frequency (w_p), the scattered photon, also known as the Stokes wave (w_S), and the acoustic phonon (Ω) is as follows,

$$w_S = w_p - \Omega \tag{2.42}$$

Conservation of momentum also requires that

$$\beta_S = \beta_p - B \tag{2.43}$$

where β_S is the wave vector for the Stokes wave, β_p is the wave vector for the pump photon, and B is the wave vector for the acoustic phonon.

The derivation for the evolution of optical power can begin with Maxwell's equations written in the form

$$\boldsymbol{\nabla}^2 E - \frac{\epsilon_L}{c^2}\frac{\partial^2 E}{\partial t^2} - \mu_o \frac{\partial^2 P_{NL}}{\partial t^2} = 0 \tag{2.44}$$

where ϵ_o is the linear dielectric constant and μ_o is the linear magnetic permeability. P_{NL} is known as the nonlinear polarization which is a result of the acousto-optic interaction and can be written as

$$P_{NL} = \frac{\gamma_e}{\rho_o}\rho E = \epsilon_o \epsilon_{NL} E \tag{2.45}$$

By replacing Eq. 2.45 into Eq. 2.44 and replacing $\epsilon_{tot} = \epsilon_L + \epsilon_{NL}$ the following is obtained

$$\boldsymbol{\nabla}^2 E = \frac{\epsilon_{tot}}{c^2}\frac{\partial^2 E}{\partial t^2} \tag{2.46}$$

where $\epsilon_{tot} = n^2(r) - in\alpha c/\omega + \epsilon_{NL}$, where the loss coefficient of the optical fiber is α. In order to come to the derivation in Equation 2.46 the following assumptions

must be made: the optical source is considered to be quasi-monochromatic; small perturbations are considered in the non-linear polarization P_{NL}.

The spatial evolution of the guided optical power for the input pump P_p and the back-scatter Stoke's wave P_s can be represented by two coupled ordinary differential equations

$$\begin{aligned} \frac{dP_p}{dz} &= -\gamma_m \zeta(\nu) P_p P_s - \alpha P_p, \\ \frac{dP_s}{dz} &= -\gamma_m \zeta(\nu) P_p P_s + \alpha P_s, \end{aligned} \tag{2.47}$$

respectively. Here α is the optical loss coefficient, ζ_m is the spectral profile of the Brillouin gain and γ_m is the peak SBS efficiency for the acoustic mode and is defined by

$$\gamma_m = \frac{g_m}{A_m^{ao}} \tag{2.48}$$

where g_m is the peak Brillouin gain and A_m^{ao} is the acousto-optic effective area. The peak Brillouin gain is given by

$$g_m = \frac{2\pi n^7 p_{12}^2}{c\lambda_p \rho_o v_a w_m}, \tag{2.49}$$

where n is the refractive index, p_{12} is the elasto-optic tensor element, c is the speed of light, λ_p is the pump wavelength, v_a is the longitudinal speed of sound and w_m is the full width at half-maximum of the Brillouin gain spectrum for the m^{th} acoustic mode. It is important to note that the elasto-optic tensor element p_{12} in Equation 2.49 is the only term that can theoretically have a value of zero.

Chapter 3

Methods and Techniques

The methods and techniques used in the production of this thesis are outlined in this chapter detailing the production of glass and the methods used to determine the material properties of these glasses.

3.1 Experimental Procedure

3.1.1 Glass Selection and Preparation

Several commercially available, optical quality glasses were selected for this study, so that precision tests could be carried out against published data on samples that are widely obtainable. In particular, glasses S-NPH3, S-TIH10, S-BSL7, made by the Ohara Corporation, as well as fused quartz, were used. Published mechanical data, as well as chemical compositions, are summarized in the following tables. Table 3.1 lists the density, ρ, longitudinal speed of sound, v_L, transverse speed of sound, v_T, index of refraction, n, and the stress-optic coefficient, C.

Table 3.1: Ohara Data Sheet Properties. The properties listed are the density (ρ), the longitudinal speed of sound (v_L), the transverse speed of sound (v_T), the index of refraction (n), and the stress-optic coefficient (C)

Name	ρ (gcm^{-3})	v_L (kms^{-1})	v_T (kms^{-1})	n (λ = 589 nm)	C (B)
S-NPH3	3.59	5.807	3.384	1.95860	3.35
S-TIH10	3.06	6.297	3.669	1.72803	2.88
S-BSL7	2.52	5.959	3.630	1.51626	2.79

The Ohara Corporation provides a general composition of some of the compounds

that the glasses investigated in this thesis are comprised of. Table 3.2 shows some of the compounds that the S-NPH3 glass is made of along with the range of the weight percent. This range does not include the main component niobium (Nb) as it does not need to be reported in the safety data sheet. The percent composition range for Nb in this glass is unknown.

Table 3.2: S-NPH3 Composition

Chemical Name	Chemical Formula	Content (Weight %)
Phosphorus pentoxide	P_2O_5	20 - 30
Titanium dioxide	TiO_2	10 - 20
Tungsten oxide	WO_3	2 - 10
Barium oxide	BaO	0 - 2
Antimony trioxide	Sb_2O_3	0 - 2

The glass composition for S-TIH10 is given in Table 3.3. The percentage of titanium dioxide (TiO_2) is of interest in this glass as it is the largest contributor to the glass properties.

Table 3.3: S-TIH10 Composition

Chemical Name	Chemical Formula	Content (Weight %)
Silicon dioxide	SiO_2	40 - 50
Titanium dioxide	TiO_2	20 - 30
Barium oxide	BaO	2 - 10
Zirconium oxide	ZrO_2	0 - 2
Calcium oxide	CaO	0 - 2
Antimony trioxide	Sb_2O_3	0 - 2

The glass composition of S-BSL7 is given in Table 3.4. This glass composition range gives a general idea of the glass composition of the main components.

These compositions are not exact compositions, however, provide a general idea of the compounds present in each glass.

The glass samples were cut to the desired dimensions using a Buehler Isomet low-speed saw with a Lapcraft Dia-Laser^{TM} diamond saw blade. After cutting samples

Table 3.4: S-BSL7 Composition

Chemical Name	Chemical Formula	Content (Weight %)
Silicon dioxide	SiO_2	60 - 70
Boron trioxide	B_2O_3	10 - 20
Barium oxide	BaO	0 - 2
Zinc oxide	ZnO	0 - 2
Antimony trioxide	Sb_2O_3	0 - 2
Titanium dioxide	TiO_2	0 - 2

were cleaned thoroughly using acetone to remove any leftover bonding material.

3.1.2 Polishing

The polishing procedure for each glass sample was performed using a Graton Vanderwilt Mico Polishing Machine, capable of polishing three samples at a time. Each sample was bonded to a mounting plate using SPI Supplies Crystalbond 509 and was then secured to the polishing machine. This machine was used to polish the optical sides of the samples where the laser beam would enter and exit.

The first polish was to 15 μm using Buehler CarbiMet^{TM} S 600 paper. After each polish, the samples and the mounts were cleaned thoroughly using ethanol. The proceeding steps used Buehler MicroCloth polishing clothes. MetaDi^{TM} Supreme polycrystalline diamond suspension was applied to the clothes for 9 μm, 6 μm, 3 μm, and then 1 μm, cleaning with ethanol between each step. The final polish was done using Buehler MasterPolish^{TM} 2 which provided a finish polish of 0.06 μm. The samples were then removed from the mounting plates and cleaned thoroughly with acetone to remove any residual polishing solution as well as any remaining Crystalbond 509.

The sides of the samples that have the acoustic wave transmitted through were initially polished using the same procedure, however, the surfaces were not uniformly flat and resulted in poor bonding to the acousto-optic setup. The samples were instead polished using the Logitech LTD PM5 Precision Lapping and Polishing System

located in the Dalhousie Microfabraction lab. Using this device the surfaces were lapped to a surface flatness of 1 um. After this, the samples were hand polished using 1 um diamond paste for an optical finish.

3.1.3 Density Measurements

The density of the glass samples was determined using Archimedes principle. The glass is first weighed in air which is recorded as the dry weight. The glass is then suspended in an 99.9 percent ethanol solution and weighted again which is recorded as its wet weight. The temperature of the ethanol is recorded as the density of ethanol is temperature-dependent. With this information, the density of the glass sample can be determined using the following equation

$$\rho_{sample} = \frac{m_{dry}}{(m_{dry} - m_{wet})}\rho_{ethanol}. \tag{3.1}$$

3.1.4 Speed of Sound Measurements

Both longitudinal and transverse velocities were determined using an Olympus 45MG Ultrasonic Thickness Gauge. The purpose of this device is to determine the thickness of a material with a known speed of sound. However, it can be used in reverse if the thickness is known to determine the speed of sound. Measuring the thickness, d, of the glass samples was done using a Vernier caliper. The ultrasonic thickness gauge measures the time between acoustic echos between reflections from the opposite surface that the transducer is attached to. The speed of sound is determined by

$$v_{L,T} = \frac{2d}{t}, \tag{3.2}$$

where t is the time for the acoustic wave to travel through the sample and be back-reflected from the other end.

3.1.5 Mechanical Properties

The mechanical properties relevant to this thesis are the Poisson ratio, ν, Young's modulus, E, shear modulus, G, and the bulk modulus, K. These values can be calculated using the density of the material, ρ, longitudinal velocity, v_L, and the transverse velocity, v_T. The mechanical properties can be calculated using the following equations

$$\nu = \frac{1 - 2(\frac{v_T}{v_L})^2}{2 - 2(\frac{v_T}{v_L})^2} \tag{3.3}$$

$$E = \frac{\rho v_T^2(3v_L^2 - 4v_T^2)}{v_L^2 - v_T^2} \tag{3.4}$$

$$G = \rho v_T^2 \tag{3.5}$$

$$K = \rho(v_L^2 - \frac{4}{3}v_T^2) \tag{3.6}$$

3.2 Abbe Refractometer

The ATAGO multi-wavelength Abbe refractometer DR-M4/1550 was used to measure the index of refraction of two of the samples. The refractometer can measure the index of refraction between 1.52 and 1.92.

A schematic representation of the refractometer is shown in Figure 3.1. The light enters the sample through a polished surface at several angles. The light is refracted towards the boundary between the sample and the main prism with a contact liquid between the two. The light is then refracted into the telescope where the boundary can be viewed. Aligning the crosshairs between the light and dark boundary allows for the measurement of the refractive index. The refractometer can be used to measure the index of refraction at wavelengths of 450 nm, 486 nm, 540 nm, 589 nm, 656 nm, and 700 nm.

The refractometer is calibrated using a test block that is provided with the device.

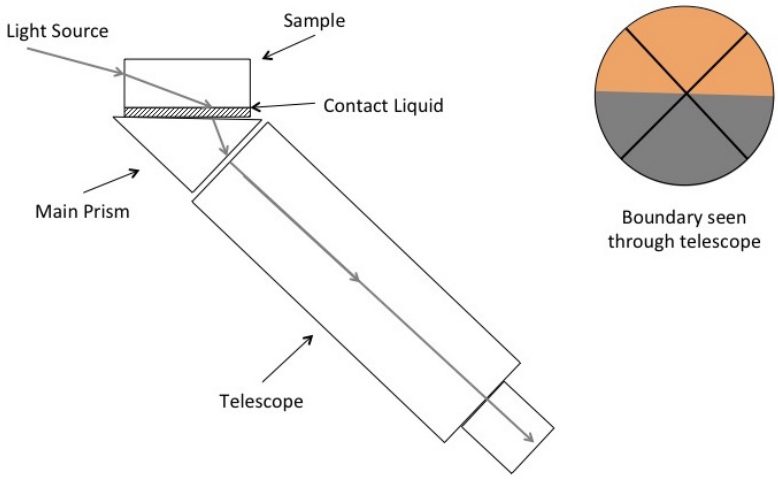

Figure 3.1: Schematic diagram of the Abbe refractometer. The sample is attached to the main prism using a contact liquid that has a higher index of refraction than the sample being measured.

The rectangular block is placed on the main prism with a contact liquid between the two surfaces. The contact liquid must have a larger refractive index compared to the sample in order to measure the refractive index. The device is calibrated at a wavelength of 589 nm. After the device is calibrated measurements at other wavelengths can be done.

The sample must have at least two sides optically polished. The front of the sample must be polished to transmit the light source into the sample. The bottom of the sample in contact with the main prism needs to be polished to transmit the light into the refractometer.

3.3 Optical Reflectance and Transmittance

Fresnel was the first to mathematically show how electromagnetic waves will be reflected and transmitted at an interface where the two mediums have a different index of refraction. If an electromagnetic wave is incident on a surface, part of the wave will be reflected and the other part will be transmitted.

Consider an incident beam of light traveling through air that strikes an interface of a medium with a larger refractive index at angle θ_i with respect to the normal. Part of the beam will be reflected at an angle θ_r and the other will be transmitted into the medium at an angle θ_t. We first consider perpendicularly polarized (s-polarized) light in which the direction of the E-field vector is perpendicular to the plane of incidence. In this case, the E-fields can be written as

$$E_{oi} + E_{or} = E_{ot} \tag{3.7}$$

where E_{oi} is the E-field of the incident beam, E_{or} is the E-field of the reflected beam into air and E_{ot} is the E-field of the transmitted beam into the medium. As well, the B-fields can be written as

$$-B_i \cos\theta_i + B_r \cos\theta_r = -B_t \cos\theta_t. \tag{3.8}$$

Using the fact that $B = En/c_o$ and the law of reflection $\theta_i = \theta_r$ and substitute these into Equation 3.8 gives

$$n_i(E_{or} - E_{oi}) \cos\theta_i = n_t E_{ot} \cos\theta_t. \tag{3.9}$$

Substituting Equation 3.7 into the above equation and rearranging results in

$$E_{or}(n_i \cos\theta_i + n_t \cos\theta_t) = E_{oi}(n_i \cos\theta_i - n_t \cos\theta_t). \tag{3.10}$$

The reflection coefficient, $r_\perp$, is then simply

$$r_\perp = \frac{E_{or}}{E_{oi}} = \frac{n_i \cos\theta_i - n_t \cos\theta_t}{n_i \cos\theta_i + n_t \cos\theta_t}. \tag{3.11}$$

Similarly, the transmission coefficient, $t_\perp$, is given by

$$t_\perp = \frac{E_{ot}}{E_{oi}} = \frac{2n_i \cos\theta_i}{n_i \cos\theta_i + n_t \cos\theta_t}. \tag{3.12}$$

Equation 3.11 and 3.12 are known as Fresnel Equations for a perpendicularly polarized incident beam.

For parallel polarization (p-polarization) the B-field is

$$B_{oi} - B_{or} = B_{ot} \tag{3.13}$$

and the E-field is given by

$$E_{oi} \cos\theta_i + E_{or} \cos\theta_r = E_{ot} \cos\theta_t. \tag{3.14}$$

Solving these equations for E_{or}/E_{oi} we obtain

$$r_\parallel = \frac{E_{or}}{E_{oi}} = \frac{n_i \cos\theta_t - n_t \cos\theta_i}{n_i \cos\theta_t + n_t \cos\theta_i}. \tag{3.15}$$

Similarly, solving for E_{ot}/E_{oi} we get

$$t_\parallel = \frac{E_{ot}}{E_{oi}} = \frac{2n_i \cos\theta_i}{n_i \cos\theta_t + n_t \cos\theta_i}. \tag{3.16}$$

Equation 3.15 and 3.16 are the Fresnel equations for parallel polarized light.

A unique case is when $\theta_i = 0$. In this case $r_\perp = r_\parallel$ and $t_\perp = t_\parallel$. In this case the Fresnel equations reduce to a much simpler form and the reflectance is given by

$$R = r^2 = \left(\frac{n_t - n_i}{n_t + n_i}\right)^2 \tag{3.17}$$

and the transmittance is given by

$$T = t^2 = \frac{4n_t n_i}{(n_t + n_i)^2}. \tag{3.18}$$

For the case of the interface between air ($n_i = 1$) and fused quartz ($n_t = 1.45$) the reflectance is approximately 3.4% and the transmittance is 96.6%. This starts to become an issue when multiple interfaces are considered such as camera lenses or when the medium has a much larger index of refraction compared to air.

3.4 Refractive Index Using Ellipsometry

The index of refraction can be measured by spectroscopic ellipsometry. The ellipsometer measures the polarization state of reflected light from a material. The light that is reflected from the materials surface is usually elliptically polarized and is represented in polar coordinates as,

$$\rho = \frac{E_{or}^{\parallel}}{E_{or}^{\perp}} = \tan\Psi e^{i\Delta}, \tag{3.19}$$

where $\tan\Psi$ is the ratio amplitude for the parallel and perpendicular polarized light measured by the detector, and Δ is the phase change between the parallel and perpendicular components of the beam.

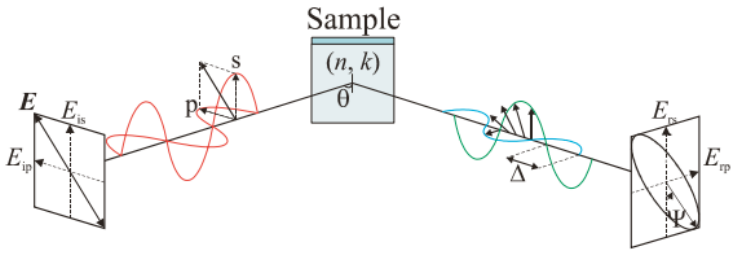

Figure 3.2: Schematic diagram of ellipsometer showing the initial polarization and the phase change, Δ, acquired by the beam after reflection. Image taken from [3]

Figure 3.2 shows a schematic representation of the incident and reflected beam.

The ellipsometer used for the measurement of the refractive index is a Woollam M-2000 variable angle spectroscopic ellipsometer located in the physics department at Dalhousie University.

The amplitude ratio can be represented by the reflection coefficients as

$$\tan\Psi = \frac{r_{\parallel}}{r_{\perp}}. \tag{3.20}$$

By solving this equation for n the index of refraction can be determined by

$$n^2 = \frac{\sin^2\theta_i(1+\tan\Psi)^2 - 4\sin^4\theta_i\tan\Psi}{\cos^2\theta_i(1+\tan\Psi)^2} \tag{3.21}$$

The data from the ellipsometer is fitted using CompleteEASE software which uses a Cauchy model to determine n. The Cauchy model used for transparent materials such as glass is

$$n(\lambda) = A + \frac{B}{\lambda^2} + \frac{C}{\lambda^4} + ... \tag{3.22}$$

The fitting of this model provides the wavelength dependence of the index of refraction, $n(\lambda)$.

3.5 Anti-Reflective Coatings on Glass

A way to overcome the reflectance loss due to Fresnel reflection at the air-glass interface is to apply anti-reflective (AR) coatings to the optical surfaces. The most basic AR coating is applying a single-layer thin film to the optical surfaces. The issue with single-layer AR coatings is they only significantly reduce the reflectance at a single-wavelength. This is because the AR coating thickness has to be a quarter of the wavelength of the incident beam wavelength. As well, in order to eliminate reflection completely the index of refraction of the AR coating needs to be equal to the square root of the index of refraction of the substrate. This is often difficult

because materials with such a low index of refraction do not exist. A commonly used AR coating material is magnesium fluoride with an index of refraction of 1.38. In the case of fused quartz as a substrate (n=1.45) this is still greater than the square root of the index of refraction. For single-layer AR coatings the thickness can be determined by

$$\lambda_o = 4n_1 d_1 \tag{3.23}$$

where λ_o is the mid-range wavelength, n_1 is the index of refraction of the AR layer, and d_1 is the layer thickness as shown in Figure 3.3 (A.). A single-layer AR coating is useful when a broad optical bandwidth is not required.

Multi-layer AR coatings are used to increase the transmittance of light through a glass over a broader wavelength range, and also over come the need for the coating material to have a low index of refraction. Only double-layer AR coatings will be considered for simplicity. For double-layer AR coatings the coating consists of a low-high refractive index coating. The order of the coatings depends on the index of refraction of the substrate. The first layer in contact with the air has a lower index of refraction (n_1) compared to the second layer (n_2) which is in contact with the substrate (n_s). For zero reflectance to occur the layer thickness of the two layers (d_1 and d_2) must satisfy the following equations

$$\frac{n_1 d_1}{\lambda_o} = \frac{1}{2\pi} \tan^{-1}\left[\pm\sqrt{YZ}\right], \tag{3.24}$$

and

$$\frac{n_2 d_2}{\lambda_o} = \frac{1}{2\pi} \tan^{-1}\left[\pm\sqrt{\frac{Y}{Z}}\right]. \tag{3.25}$$

There is a requirement that

$$YZ > 0, \tag{3.26}$$

where

$$Y = \frac{n_1 n_2 (n_o - n_s)}{n_o n_2^2 - n_1^2 n_s}, \tag{3.27}$$

and

$$Z = \frac{n_1 (n_o n_s - n_2^2)}{n_2 (n_1^2 - n_0 n_s)}. \tag{3.28}$$

Equation 3.26 requires that Y and Z both be positive or both be negative. Substituting Equations 3.27 and 3.28 into Equations 3.24 and 3.25 results in the following

$$\frac{n_1 d_1}{\lambda_o} = \frac{1}{2\pi} \tan^{-1} \left[\pm \sqrt{\frac{n_1^2 (n_o - n_s)(n_o n_s - n_2^2)}{(n_o n_2^2 - n_1^2 n_s)(n_1^2 - n_o n_s)}} \right], \tag{3.29}$$

$$\frac{n_2 d_2}{\lambda_o} = \frac{1}{2\pi} \tan^{-1} \left[\pm \sqrt{\frac{n_2^2 (n_o - n_s)(n_1^2 - n_o n_s)}{(n_o n_2^2 - n_1^2 n_s)(n_o n_s - n_2^2)}} \right]. \tag{3.30}$$

These equations can be used to determine the layer thickness of the AR coatings, however, the following requirements must be true. If Y and Z are positive then both signs in Equations 3.29 and 3.30 are positive. If Y and Z are negative then these signs are different. The layer thicknesses are shown in Figure 3.3 (B.).

3.6 Electron-Beam Physical Vapour Deposition

Electron-beam physical vapour deposition (EBPVD) is a method of applying thin film coatings to surfaces. The fused quartz samples used were coated using this technique by BMV Optical Technologies to reduce reflection losses at the air-glass interface.

The setup used was a standard (EBPVD) where the material to be deposited on the surface of the sample is radiated by an electron-beam gun. This results in the deposited material being vapourized which then deposits onto the surface of the sample. This method allows the layers to be deposited on the sample in a controlled way to achieve the desired thickness of the film. By tailoring the deposited film material and the thickness the optical loss due to reflectance at the air-glass interface

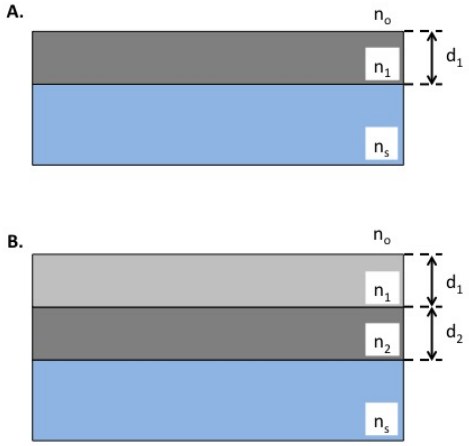

Figure 3.3: (A.) Single-layer AR coating where n_o is the index of refraction of air, n_1 is the index of refraction of the AR coating, d_1 is the coating thickness, and n_s is the index of refraction of the substrate (glass). (B.) Double-layer AR coating where n_1 is the index of refraction of the first layer, d_1 is the thickness of the first layer, n_2 is the index of refraction of the second layer in contact with the substrate, and d_2 is the layer thickness of the second layer.

can be reduced.

3.7 Sénarmont Compensator

3.7.1 Polarization

Most light sources are unpolarized meaning the electric field oscillates in all directions. The magnetic field also oscillates in the same way and is perpendicular to the electric field such that the direction of propagation is in the direction $\mathbf{E} \times \mathbf{B}$.

Polarized light consists of an optical beam that only has an electric field oscillating in a single direction. This is only possible if light is a transverse wave and the fact that it can be polarized proves that it is such [37].

Consider a light ray traveling in the direction out of the page (z-direction) with the E-field oscillating in the x- and y-directions as shown in Figure 3.4. The E-field

depicted in Figure 3.4 can be represented as unit vectors **i** and **j**

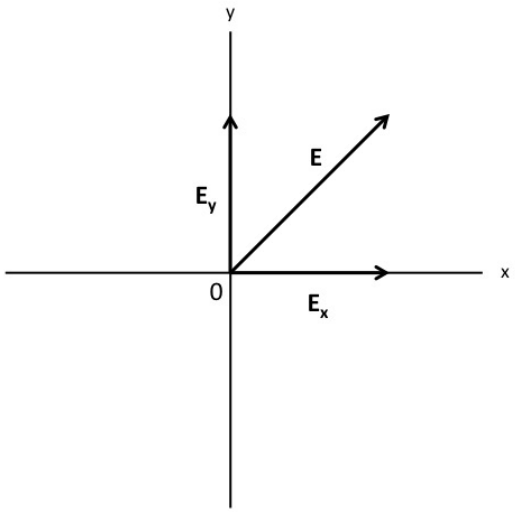

Figure 3.4: Instantaneous E-field oscillating in the x- and y-directions with the light ray traveling in the +z-direction.

$$\mathbf{E} = \mathbf{i}E_x + \mathbf{j}E_y \tag{3.31}$$

where E_x and E_y are the electric field in the x and y direction. With time and spatial dependence of the E-field components one obtains,

$$E_x = E_{ox}e^{i(kz-wt+\varphi_x)} \tag{3.32}$$

and

$$E_y = E_{oy}e^{i(kz-wt+\varphi_y)}. \tag{3.33}$$

For waves traveling in the +z-direction that have amplitude E_{ox} and E_{oy}, with phases φ_x and φ_y our definition of the E-field in Eq. 3.31 becomes

$$\mathbf{E} = \mathbf{i}E_{ox}e^{i(kz-wt+\varphi_x)} + \mathbf{j}E_{oy}e^{i(kz-wt+\varphi_y)} \tag{3.34}$$

or it may also be written as

$$\mathbf{E} = [\mathbf{i}E_{ox}e^{i\varphi_x} + \mathbf{j}E_{oy}e^{i\varphi_y}]e^{kz-wt} = \tilde{E}_o e^{i(kz-wt)} \tag{3.35}$$

where the complex amplitude of the polarized wave is denoted by $\tilde{E}_o = \mathbf{i}E_{ox}e^{i\varphi_x} + \mathbf{j}E_{oy}e^{i\varphi_y}$. Polarized light can be represented by what are known as Jones matrices which was developed by R. Clark Jones in 1942 [38]. In order to describe the polarization of light one needs only to focus on the amplitude and phase of these components which may be written as Jones vectors in the following way

$$\tilde{E}_o = \begin{bmatrix} \tilde{E}_{ox} \\ \tilde{E}_{oy} \end{bmatrix} = \begin{bmatrix} E_{ox}e^{i\varphi_x} \\ E_{oy}e^{i\varphi_y} \end{bmatrix} \tag{3.36}$$

In this thesis two types of polarization are considered: horizontally polarized light which is considered to have the electric field oriented parallel to the Earth's surface, and vertically polarized light where the electric field is oriented perpendicular to the Earth's surface. Table 3.5 shows the appropriate Jones matrices relevant to the optical systems described in this thesis.

Table 3.5: Jones matrices. The following table lists the Jones matrices relevant to this thesis.

Optical element	Jones matrix
Linear Polarizer at ±45deg "L(±45)"	$\frac{1}{2}\begin{bmatrix} 1 & \pm 1 \\ \pm 1 & 1 \end{bmatrix}$
Quarter-Wave Plate with fast axis oriented along x-axis "Q(x)"	$e^{i\pi/4}\begin{bmatrix} 1 & 0 \\ 0 & i \end{bmatrix}$
Rotation Matrix "R(θ)"	$\begin{bmatrix} \cos\theta & \sin\theta \\ -\sin\theta & \cos\theta \end{bmatrix}$

3.7.2 Sénarmont Compensator Theory

The Sénarmont compensator is a device used to measure the retardation of light as it passes through a material. These measurements can be used to measure the stress-optic coefficient of glass samples and the photoelastic response under strain. The Sénarmont compensator is comprised of a laser, polarizer, sample mount, quarter-wave plate, analyzer, and detector. The laser beam is polarized at 45^o to the x- and y-axes. The electric field of the beam is represented as

$$\mathbf{E}(z,t) = E_o e^{i(kz-wt)}(\hat{x}+\hat{y}) \tag{3.37}$$

When the beam travels through a sample of thickness d that is stressed the electric field becomes

$$\mathbf{E}(z+d,t) = E_o e^{i(kz-wt)}(e^{ik_o d}\hat{x}+e^{ik_e d}\hat{y}) \tag{3.38}$$

where,

$$k_o = \frac{2\pi n_o}{\lambda}, k_e = \frac{2\pi n_e}{\lambda} \tag{3.39}$$

Substituting this into Equation 3.38 and rearranging gives

$$\mathbf{E}(z+d,t) = E_o e^{(kz-wt)} e^{i2\pi n_o d/\lambda}(\hat{x}+e^{i2\pi(n_e-n_o)d/\lambda}\hat{y}) \tag{3.40}$$

The phase change, Δ, between the x and y components can be related to the stress-optic coefficient by

$$\Delta = \frac{2\pi d(n_e-n_o)}{\lambda} = \frac{2\pi d}{\lambda} C\sigma \tag{3.41}$$

In order to determine the stress-optic coefficient the change in the polarization as the beam passes through a stressed sample needs to be analyzed. It is beneficial to use

Jones matrices to analyze what happens to the beam as it traverses the Sénarmont setup. The light exiting the glass can be rewritten as a Jones matrix

$$\mathbf{E} = E_o e^{i\Delta/2} \begin{bmatrix} e^{-i\Delta/2} \\ e^{i\Delta/2} \end{bmatrix} \tag{3.42}$$

The Jones matrices used for the calculation are listed in Table 3.5. After the beam exits the stressed glass it encounters a quarter-wave plate with its fast axis set parallel to $(\hat{x} + \hat{y})$. The electric field of the beam as it passes through the quarter-wave plate can be written as

$$\mathbf{E} = R(-45^o)Q(x)R(45^o)E_o e^{i\Delta/2} \begin{bmatrix} e^{-i\Delta/2} \\ e^{i\Delta/2} \end{bmatrix} \tag{3.43}$$

Substituting the appropriate Jones matrices from Table 3.5 and simplifying, the electric field exiting the quarter-wave plate becomes

$$\mathbf{E} = E_o e^{i\pi/4} e^{i\Delta/2} \begin{bmatrix} \cos(\Delta/2) + \sin(\Delta/2) \\ \cos(\Delta/2) - \sin(\Delta/2) \end{bmatrix} \tag{3.44}$$

The beam then encounters the analyzer which is initially aligned perpendicular to the incident light at $\pm(\hat{x} - \hat{y})$ axis. The analyzer is then rotated to an angle θ to find the minimum intensity. The electric field is represented by

$$\mathbf{E} = R(-\theta)L(-45^o)R(\theta)E_o e^{i\pi/4} e^{i\Delta/2} \begin{bmatrix} \cos(\Delta/2) + \sin(\Delta/2) \\ \cos(\Delta/2) - \sin(\Delta/2) \end{bmatrix} \tag{3.45}$$

Again, substituting the appropriate Jones matrices from Table 3.5 and simplifying, the electric field exiting the analyzer is

$$\mathbf{E} = \frac{1}{2} E_o e^{i\pi/4} e^{i\Delta/2} \begin{bmatrix} \cos(\Delta/2) + \sin(\Delta/2) + \sin(2\theta + \Delta/2) - \cos(2\theta + \Delta/2) \\ \cos(\Delta/2) - \sin(\Delta/2) - \sin(2\theta + \Delta/2) - \cos(2\theta + \Delta/2) \end{bmatrix} \quad (3.46)$$

For a generalized light wave, $\mathbf{A} = \begin{bmatrix} A_x \\ A_y \end{bmatrix}$, the intensity can be written as $I = A_x^2 + A_y^2$. Thus, the intensity of the light at the detector is

$$I = 4 - 4\cos(2\theta + \Delta) \quad (3.47)$$

If the intensity is a minimum ($I = 0$) then the phase change becomes

$$\Delta = -2\theta \pm \frac{\pi}{2} \quad (3.48)$$

Therefore, using the Sénarmont setup the minimum angles can be found for a given stress and the phase change can be calculated. Using this along with Equation 3.41 the stress-optic coefficient can be determined.

3.7.3 Sénarmont Compensator Measurements

The stress-optic coefficient was measured using the Sénarmont compensator method described in Section 3.7. The Sénarmont setup is shown in Figure 3.5.

The Sénarmont setup up is comprised of a 670 nm laser, a Glan-Taylor linear polarizer, the sample mount that applies a uniaxial stress, a liquid crystal variable retarder (LCVR), an analyzer, and a power detector. The incident beam is polarized at 45^o with respect to the x and y axis. As the light passes through the stressed sample the beam acquires a phase change between the x- and y-components and becomes elliptically polarized. The LCVR can be used as a $\lambda/4$-plate which is used to convert

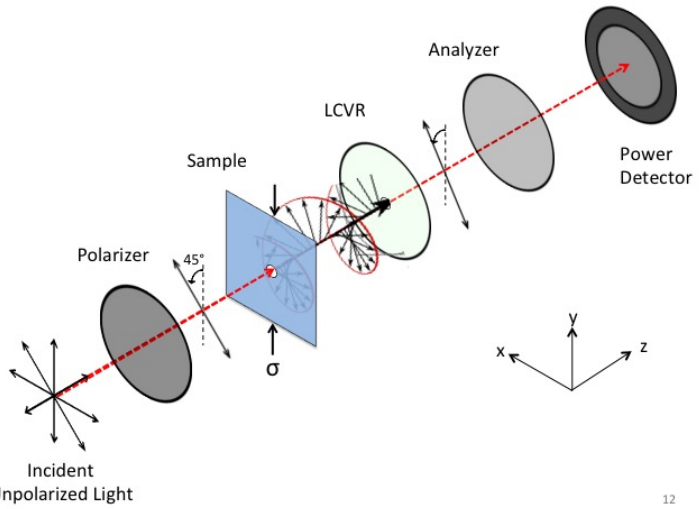

Figure 3.5: The Sénarmont compensator. The light is initially polarized at 45^o to the x and y axes and undergoes a phase change as it passes through the stressed sample. The phase change is then measured at the power detector.

the elliptically polarized light back into linearly polarized light. By measuring the output of the power detector at different angles of the analyzer the angle of minimum intensity can be obtained. These angles along with the stress at which they occur can be used to obtain a linear graph of the phase change versus applied stress. Using the slope of this graph along with Equation 3.41 the stress-optic coefficient can be determined.

3.8 Photoelastic Measurements

The photoelastic measurements were determined using the Dixon-Cohen method which was first used to investigate the photoelastic properties of Lithium Niobate crystals [30].

This thesis employs the Dixon-Cohen method for the measurement of the photoelastic constants of glass which was first published by R. W. Dixon and M. G. Cohen [30]. This method uses the acousto-optic effect described in Section 2.3. A laser beam

incident on the quartz reference piece at the Bragg angle is diffracted by the injected acoustic wave as shown in Figure 3.6 where the laser beam is depicted traversing through the sample. The diffracted beam intensity is measured by a photodiode and produces a time-dependent intensity as shown in Figure 3.7. The intensity peaks of interest are labeled I_1 and I_R which is the initial acoustic wave diffraction and the acoustic wave diffraction from the acoustic wave that is transmitted into the sample and reflected from the free end and is re-transmitted back into the reference piece respectively.

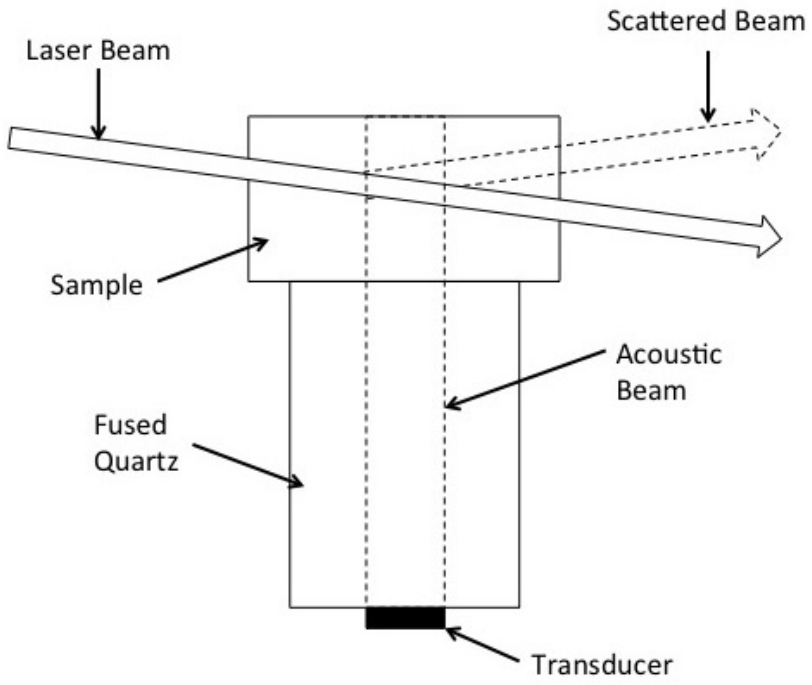

Figure 3.6: The acoustic wave travels through the fused quartz and is transmitted into the sample where the incident laser beam is diffracted by the acoustic wave.

The same procedure occurs in the glass sample where the acoustic wave is transmitted into the sample from the reference piece. The intensity peaks of interest are labeled I_4 and I_5 which is the initially injected acoustic wave into the sample and the reflected acoustic wave from the free end respectively. These intensities can be used to calculate p_{11} and p_{12} of the sample using Equation 2.41. This requires the

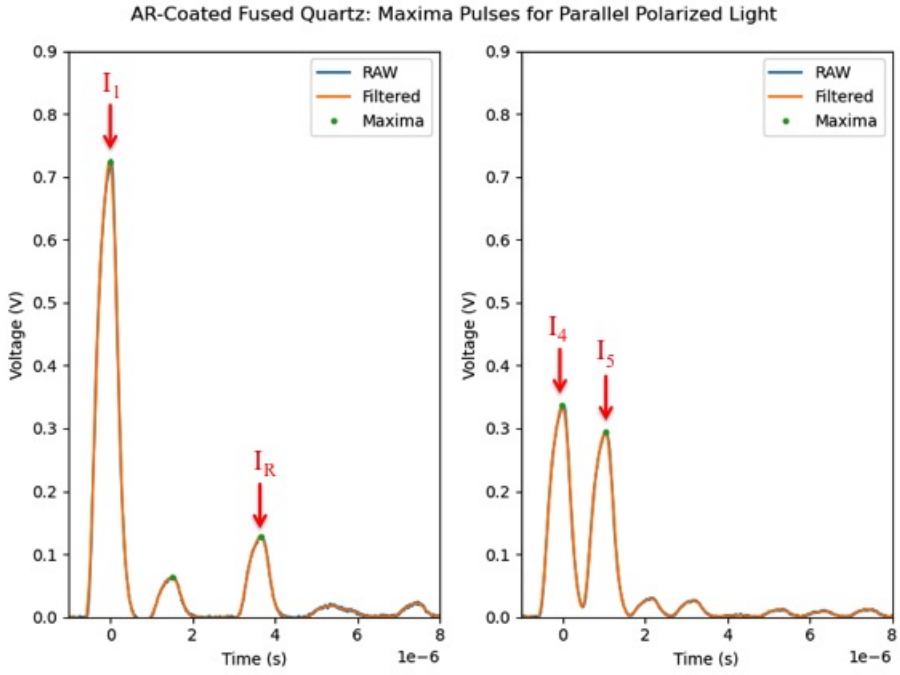

Figure 3.7: The acoustic wave travels through the fused quartz and is transmitted into the sample where the incident laser beam is diffracted by the acoustic wave. The left graph is the data collected when the laser is passing through the reference and the right graph is when the laser is passing through the sample.

photoelastic coefficients of fused quartz to be known which have been taken from Ref. [39] at 632 nm wavelength.

The Dixon-Cohen setup is comprised of a 670 nm laser which is polarized vertically or horizontally polarized. The polarized light passes through a pinhole to reduce the beam size to < 1 mm. The laser beam hits the acousto-optic device made by AA Opto-electronic at the Bragg angle defined by

$$\theta_B = \sin^{-1}(\frac{\lambda}{2\Lambda}) \tag{3.49}$$

where θ_B is the Bragg angle, λ is the laser beam wavelength, and Λ is the acoustic

wavelength. The laser beam is diffracted at the Bragg angle as it leaves the acousto-optic device. A second pinhole is used to block the undiffracted beam. The diffracted laser beam is measured using a photodiode detector. The photodiode detector is connected to a 200 MHz Tetronix oscilloscope. A schematic diagram is shown in Figure 3.8.

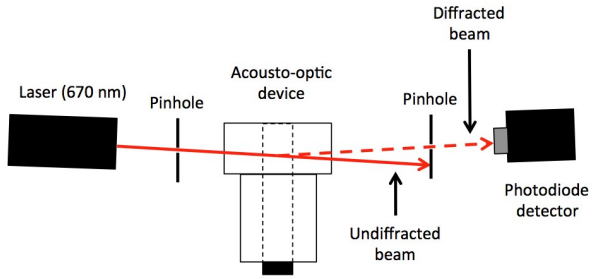

Figure 3.8: Schematic representation of the Dixon Cohen setup used to measure the photoelastic coefficients of glass samples

Chapter 4

Results

4.1 Mechanical Properties

The mechanical properties of the glass samples were determined by measuring the speed of sound using the ultrasonic thickness gauge described in Section 3.1.4 and the density described in Section 3.1.3 along with index of refraction measurements taken using an Abbe refractometer and an ellipsometer. The values are listed in Table 4.1. All glasses have similar longitudinal and transverse speeds of sound. The uncertainty for all values given in Table 4.1 was determined by the standard deviation of ten individual measurements with the exception of the index of refraction measurements for Fused Quartz and S-NPH3 which were determined by the fitting of the ellipsometer data.

Table 4.1: Measured Properties. Here the density (ρ), longitudinal speed of sound (v_L), transverse speed of sound (v_T), and index of refraction (n) are presented.

Name	ρ (gcm^{-3})	v_L (kms^{-1})	v_T (kms^{-1})	n (λ = 589 nm)
Fused Quartz	2.194 ± 0.008	5.950 ± 0.008	3.770 ± 0.010	1.466 ± 0.005
S-NPH3	3.573 ± 0.009	5.831 ± 0.009	3.405 ± 0.005	1.931 ± 0.005
S-TIH10	3.035 ± 0.009	5.929 ± 0.005	3.438 ± 0.006	1.7299 ± 0.0003
S-BSL7	2.507 ± 0.006	6.013 ± 0.005	3.660 ± 0.010	1.5171 ± 0.0001

By measuring the speed of sound and the density the Young's modulus (E), shear modulus (G), bulk modulus (K), and Poisson ratio (ν) can be calculated using Equation's 3.3 - 3.6. These values are listed in Table 4.2. The uncertainty of all values given in Table 4.2 was determined by error propagation.

Table 4.2: Mechanical Properties. The following table lists Young's modulus (E), shear modulus (G), bulk modulus (K), and Poisson ratio (ν).

Name	E (GPa)	G (GPa)	K (GPa)	ν
Fused Quartz	72.6 ± 0.3	31.2 ± 0.2	36.1 ± 0.3	0.165 ± 0.003
S-NPH3	102.8 ± 0.5	41.4 ± 0.2	66.3 ± 0.4	0.241 ± 0.002
S-TIH10	89.4 ± 0.3	35.9 ± 0.2	58.7 ± 0.3	0.246 ± 0.001
S-BSL7	81.0 ± 0.4	33.6 ± 0.2	45.9 ± 0.3	0.206 ± 0.003

4.2 Index of Refraction Results

The wavelength dependence for fused quartz and the three Ohara glasses are shown in Figures 4.1 - 4.4. The index of refraction for fused quartz and S-NPH3 were measured using an ellipsometer due to the limitations of the Abbe refractometer used for the other measurements. The index of refraction for S-TIH10 and S-BSL7 were measured using the Abbe refractometer at six separate wavelengths and compared to the measurements provided by Ohara in the glass data sheets.

The wavelength dependence of fused quartz is shown between approximately 200 nm to 1000 nm in Figure 4.1. As expected based on the Cauchy model the index of refraction decreases with increasing wavelength.

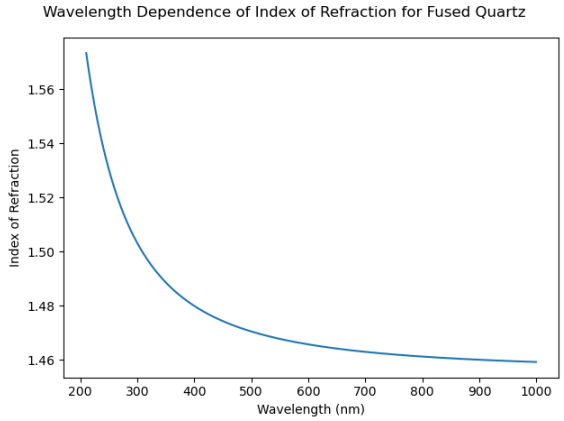

Figure 4.1: The index of refraction for fused quartz decreases as the wavelength increases

The index of refraction for S-NPH3 is shown between 400 nm to 1000 nm in Figure

4.2. The index of refraction decreases as the wavelength increases. This is the typical response of transparent materials.

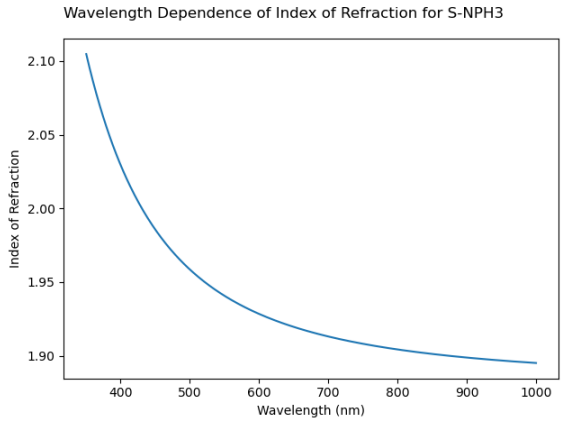

Figure 4.2: The index of refraction for S-NPH3 decreases as the wavelength increases

The index of refraction for S-TIH10 is shown in Figure 4.3 for six wavelengths: 450 nm, 486 nm, 540 nm, 589 nm, 656 nm, and 700 nm. These are graphed alongside the provided index of refraction measurements given in the Ohara data sheets. The measured index of refraction are slightly higher than the reported index of refraction by Ohara.

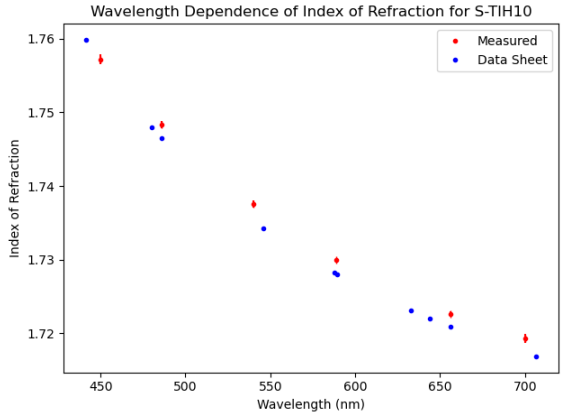

Figure 4.3: The index of refraction for S-TIH10 decreases as the wavelength increases. There is a systematic difference between the measured values and the literature values due to the contact liquid being used.

The index of refraction is shown for S-BSL7 for six wavelengths; 450 nm, 486

nm, 540 nm, 589 nm, 656 nm, and 700 nm. Again the index of refraction measured are slightly higher than the reported index of refraction provided by the Ohara data sheet.

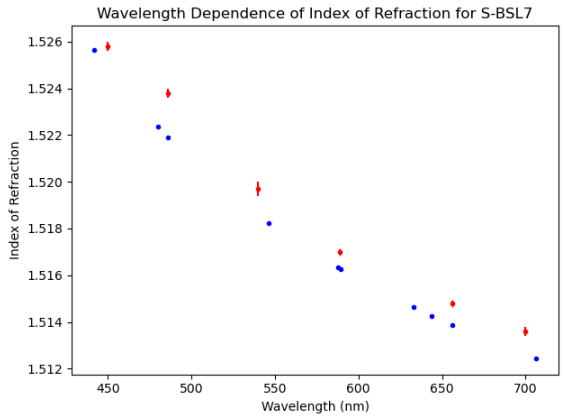

Figure 4.4: The index of refraction for S-BSL7 decreases as the wavelength increases. There is a systematic difference between the measured values and the literature values due to the contact liquid being used.

4.3 Sénarmont Compensator Results

The data from the Sénarmont compensator is shown in Figures 4.5 - 4.8. The graphs show the phase change versus the applied stress for each glass sample using a 670 nm laser. The slope of each graph is used to determine the stress-optic coefficient. The uncertainty for the stress-optic coefficient comes from the slope of the graph. All graphs show a linear trend with minimal error. The stress-optic coefficient can be calculated from the slope of the line using Equation 3.41. The error in the stress-optic coefficient is determined by the uncertainty in the slope of the linear fit and through error propagation.

Figure 4.5 shows the Sénarmont data for fused quartz. The sample is stressed between -1.5 MPa and -3.0 MPa. As the applied stress decreases the phase change decreases towards zero.

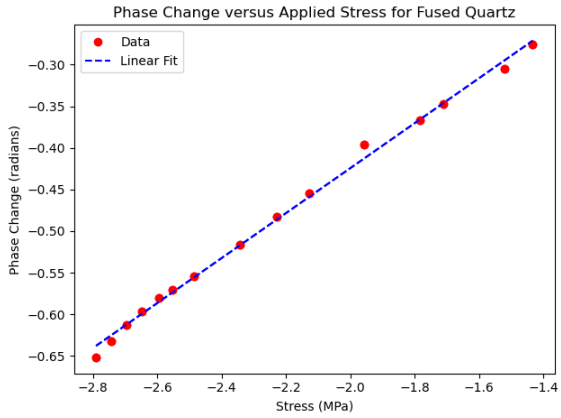

Figure 4.5: The phase change Δ for 670 nm as a function of stress σ for fused quartz. The slope of Δ vs σ is used to determine the stress optic coefficient

Figure 4.6 shows the Sénarmont data for S-NPH3. The stress on the sample is higher compared to fused quartz due to the dimensions of the S-NPH3 being smaller and therefore the force per unit area being higher. This data shows a clear linear trend towards zero with decreasing phase change as the stress on the sample decreases.

Figure 4.7 shows the Sénarmont data for S-TIH10 which is stressed between -3.0

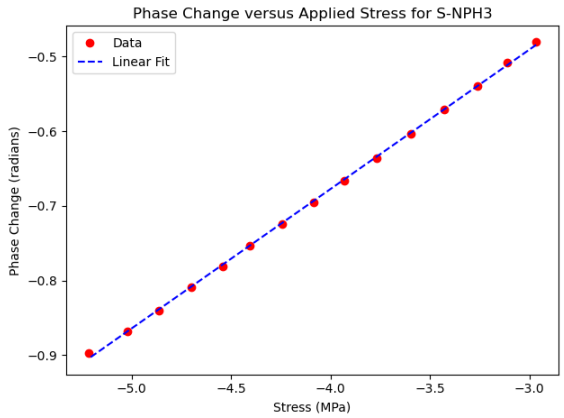

Figure 4.6: The phase change Δ for 670 nm as a function of stress σ for S-NPH3. The slope of Δ vs σ is used to determine the stress optic coefficient

MPa and -5.5 MPa, similar to S-NPH3. Both samples have approximately the same dimensions.

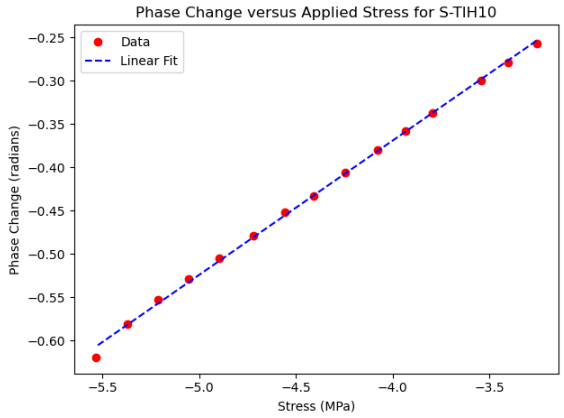

Figure 4.7: The phase change Δ for 670 nm as a function of stress σ for S-TIH10. The slope of Δ vs σ is used to determine the stress optic coefficient

The Sénarmont data for S-BSL7 is shown in Figure 4.8 where the stress is slightly less compared to S-NPH3 and S-TIH10. This is due to how the sample was initially stressed and was not given sufficient time to relax so the data points above -4.5 MPa were ignored and more data points at lower stress were taken.

The calculated stress-optic coefficients are presented in Table 4.3. All glasses show a large positive stress-optic coefficient. The Sénarmont data is not considered

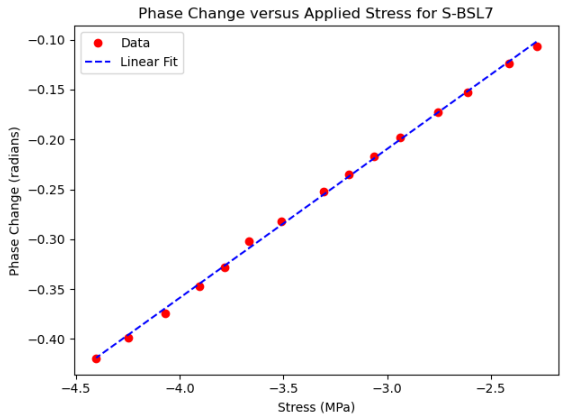

Figure 4.8: The phase change Δ for 670 nm as a function of stress σ for S-BSL7. The slope of Δ vs σ is used to determine the stress optic coefficient

reliable for the accurate determination of the stress-optic coefficient, only whether it is positive or negative. This is due to the inability to obtain a uniform stress throughout the sample. In this case the measured stress may vary from the actual stress at the location of the laser beam.

Table 4.3: Stress-Optic Coefficients Measured Using Sénarmont Compensator Method

Name	C (B)
Fused Quartz	3.15 ± 0.05
S-NPH3	3.36 ± 0.02
S-BSL7	2.31 ± 0.02
S-TIH10	2.46 ± 0.03

4.4 Acousto-Optic Results

The scattered beam intensities from the acousto-optic setup are shown in Figure 4.9-4.16 for fused quartz, AR-coated fused quartz, and the three Ohara glass samples at a wavelength of 670 nm.

A fused quartz sample is bonded to the reference fused quartz to determine the accuracy of the setup. The scattered beam intensities for the fused quartz sample and the reference are shown in Figures 4.9 and 4.10 for light polarized parallel and perpendicular to the acoustic beam, respectively. Figure 4.9 (left) shows the scattered intensity as the laser beam travels through the reference piece of the acousto-optic setup. Figure 4.9 (right) shows the scattered beam intensities as the laser beam travels through the uncoated fused quartz sample.

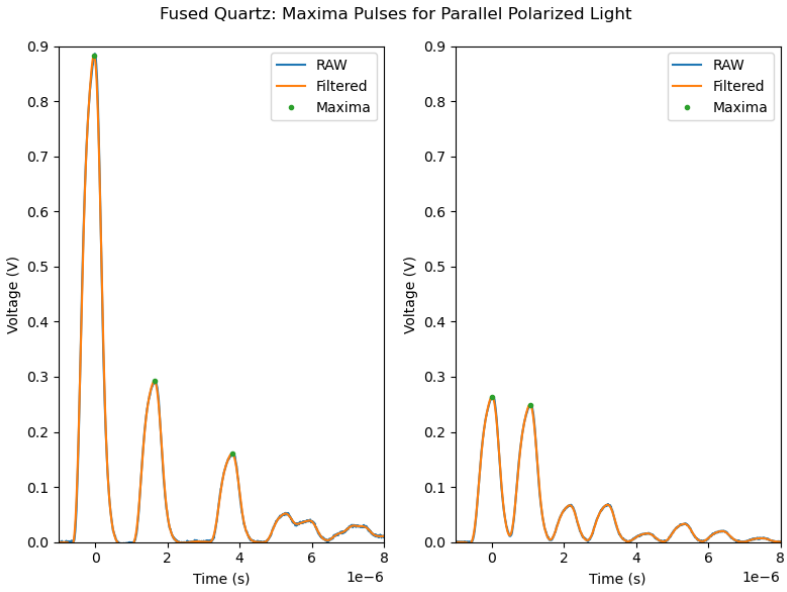

Figure 4.9: Scattered beam intensity from the uncoated fused quartz sample with laser beam polarized parallel to the acoustic wave. (Left) shows the laser beam scattering through the reference. (Right) shows the laser beam scattering through the fused quartz sample

The scattered beam intensities for the AR-coated fused quartz sample are shown in Figure 4.11 and 4.12. The transmission of the acoustic wave into the AR-coated

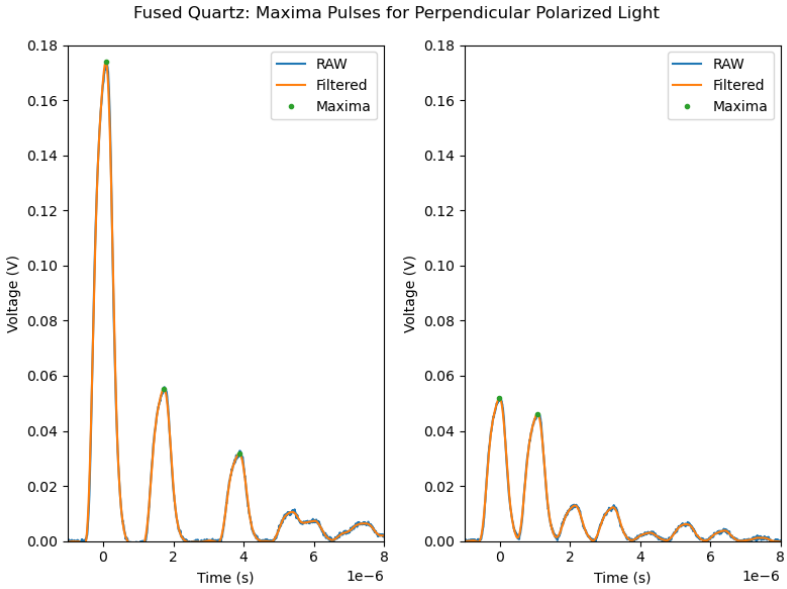

Figure 4.10: Scattered beam intensity from the uncoated fused quartz sample with laser polarized perpendicular to the acoustic wave

fused quartz sample is significantly better compared to the uncoated fused quartz sample.

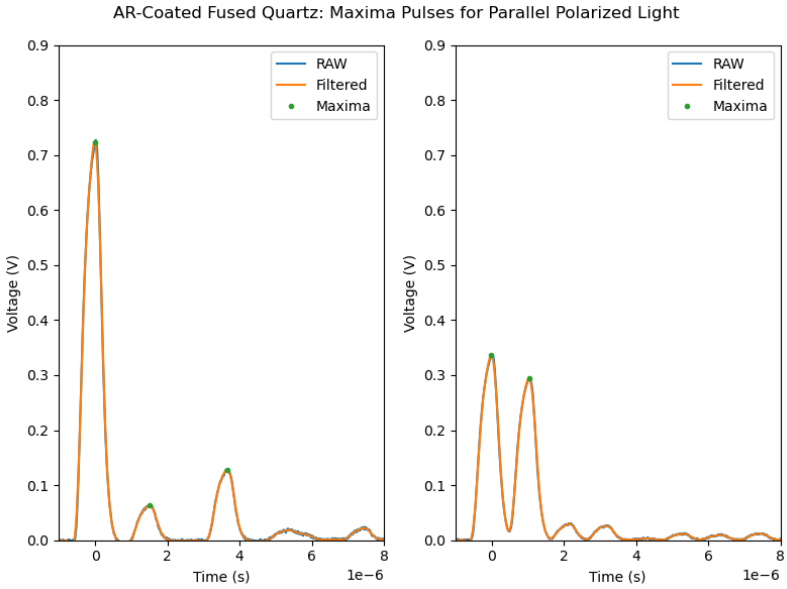

Figure 4.11: Scattered beam intensity from AR-coated fused quartz sample with laser beam polarized parallel to the acoustic wave

The scattered beam intensities for the S-NPH3 sample are shown in Figure 4.13

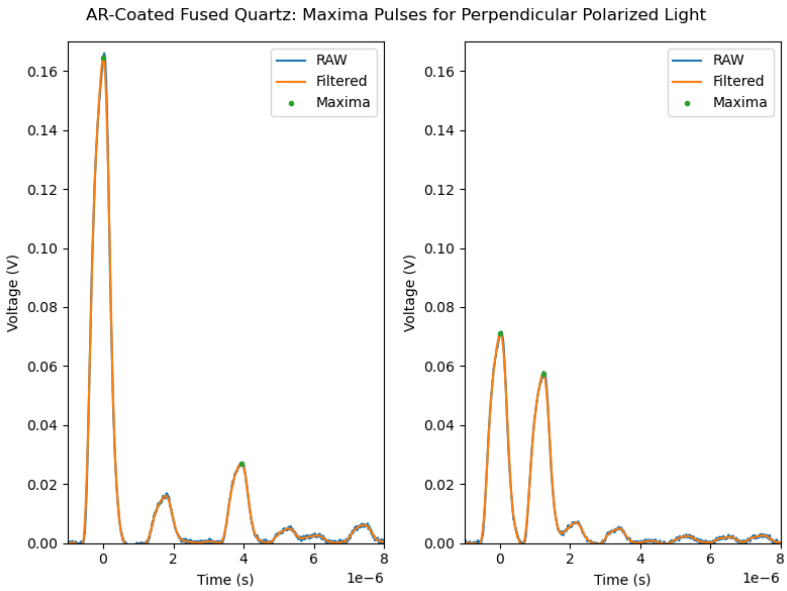

Figure 4.12: Scattered beam intensity from AR-coated fused quartz sample with laser polarized perpendicular to the acoustic wave

and 4.14. Figure 4.13 shows the scattered beam intensities through the reference and the sample for light polarized parallel to the acoustic wave. Figure 4.14 shows the scattered beam intensities through the reference and the sample for light polarized perpendicular to the acoustic wave.

The scattered beam intensities for S-BSL7 are shown in Figure 4.15 and 4.16. The transmission of the acoustic wave into the S-BSL7 sample was less compared to that of the AR-coated fused quartz and the S-NPH3 sample.

The individual photoelastic tensor elements and the stress-optic coefficient are presented in Table 4.4. The photoelastic tensor elements could only be measured for uncoated fused quartz, AR-coated fused quartz, S-BSL7 and S-NPH3 samples. S-TIH10 could not be measured due to surface flatness problems.

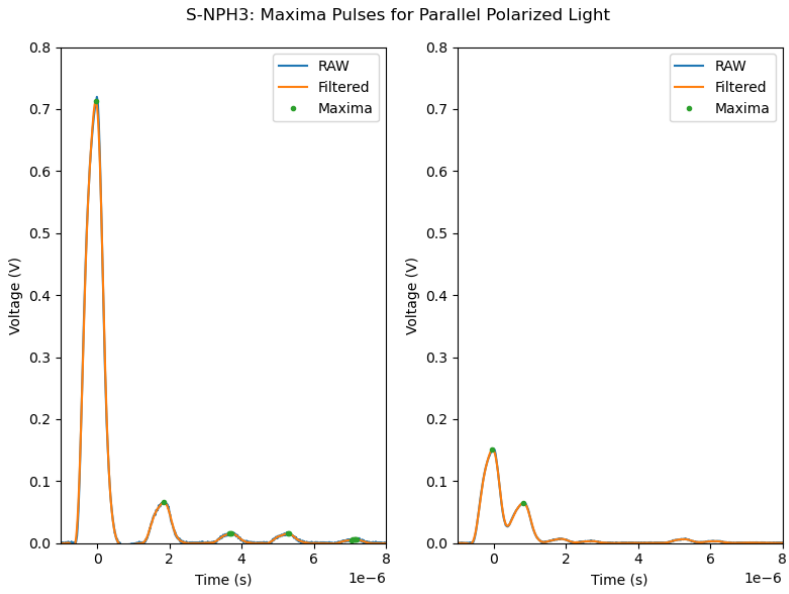

Figure 4.13: Scattered beam intensity from fused quartz reference with S-NPH3 sample attached with laser beam polarized parallel to the acoustic wave

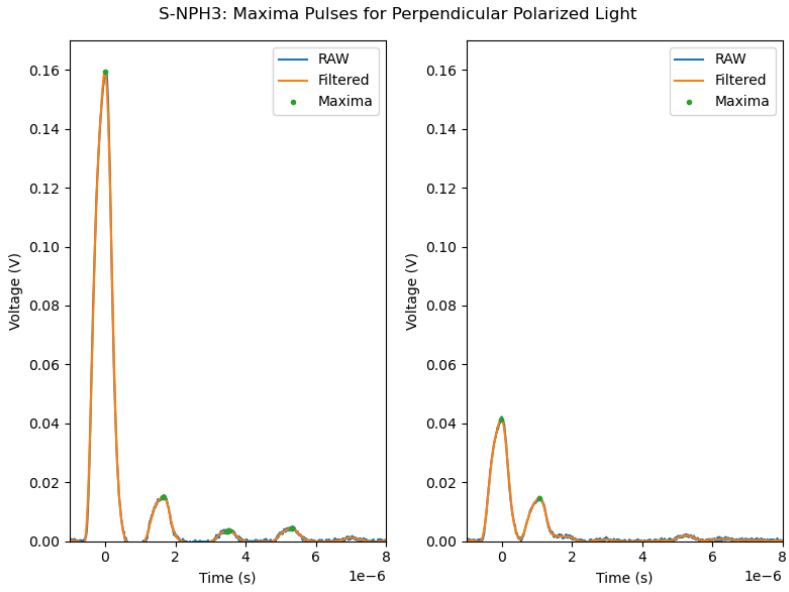

Figure 4.14: Scattered beam intensity from S-NPH3 sample with laser beam polarized perpendicular to the acoustic wave

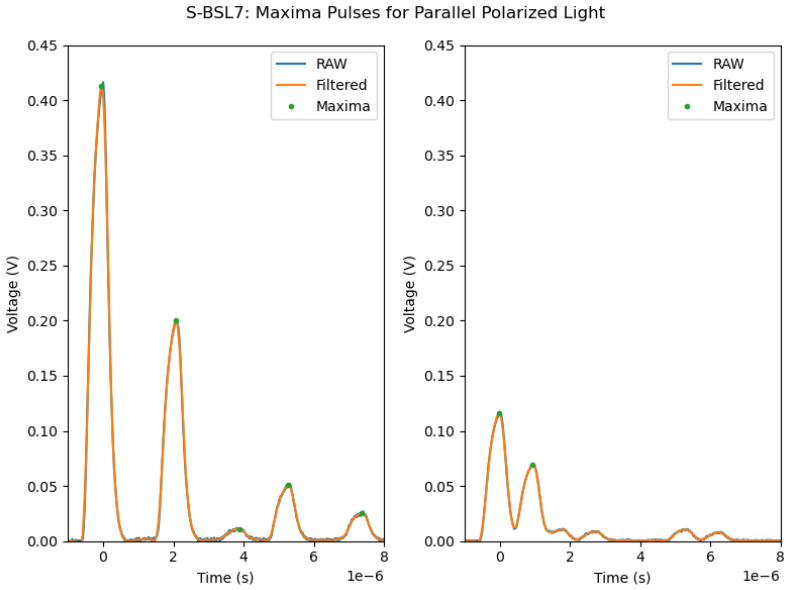

Figure 4.15: Scattered beam intensity from S-BSL7 sample with laser beam polarized parallel to the acoustic wave

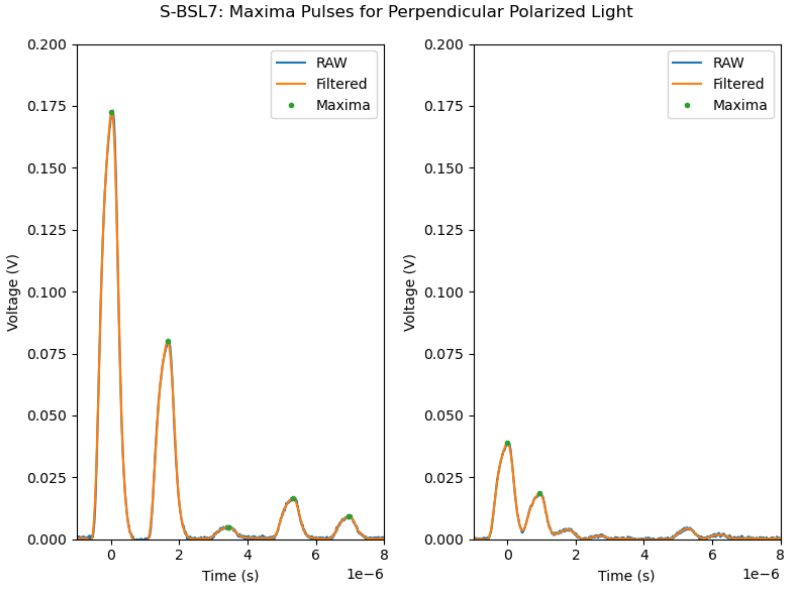

Figure 4.16: Scattered beam intensity from S-BSL7 sample with laser beam polarized perpendicular to the acoustic wave

Table 4.4: Photoelastic Properties. p_{11} and p_{12} are the individual photoelastic tensor elements, and C is the stress-optic coefficient.

Name	p_{11}	p_{12}	C (B)
Fused Quartz	0.100 ± 0.002	0.219 ± 0.003	3.0 ± 0.1
AR-Coated Fused Quartz	0.123 ± 0.004	0.264 ± 0.008	3.5 ± 0.2
S-NPH3	0.064 ± 0.001	0.152 ± 0.004	3.7 ± 0.2
S-BSL7	0.136 ± 0.001	0.254 ± 0.003	3.0 ± 0.1

Chapter 5

Discussion

5.1 Discussion of Results

The speed of sound measurements for the glass samples were all within 1% of the expected values with the exception of S-TIH10. Table 3.1 shows the reported values from the Ohara Corporation data sheets. The expected speed of sound for S-TIH10 was 3669 m/s for the transverse and 6296 m/s for the longitudinal. Comparing these values to the values measured in Table 4.1 there is a greater than 5% disagreement. Comparing the density measured for S-TIH10 to the expected value is close to the uncertainty of the measurement so it can be assumed that the sample is the correct composition provided by Ohara. After contacting the company this discrepancy has yet to be resolved. The assumption made in this thesis is that the speed of sound measurements for S-TIH10 are incorrectly reported in the data sheet from Ohara.

The index of refraction for all four glasses decreased with wavelength which is to be expected based on the Cauchy model described in Equation 3.22. The index of refraction for fused quartz and S-NPH3 were measured using the ellipsometer because the index of refraction was too low or too high for the Abbe refractometer to measure. S-BSL7 and S-TIH10 were within the limits of the Abbe refractometer. Comparing the index of refraction to the reported index of refraction in Table 3.1 both S-BSL7 and S-TIH10 all measured index of refraction values are above the reported values as shown in Figure 4.4 and Figure 4.3. This indicates that there is a systematic error in the measurement. It is possible that the contact liquid slightly shifts the index of refraction. The contact liquid used was old, purchasing a new contact liquid may help

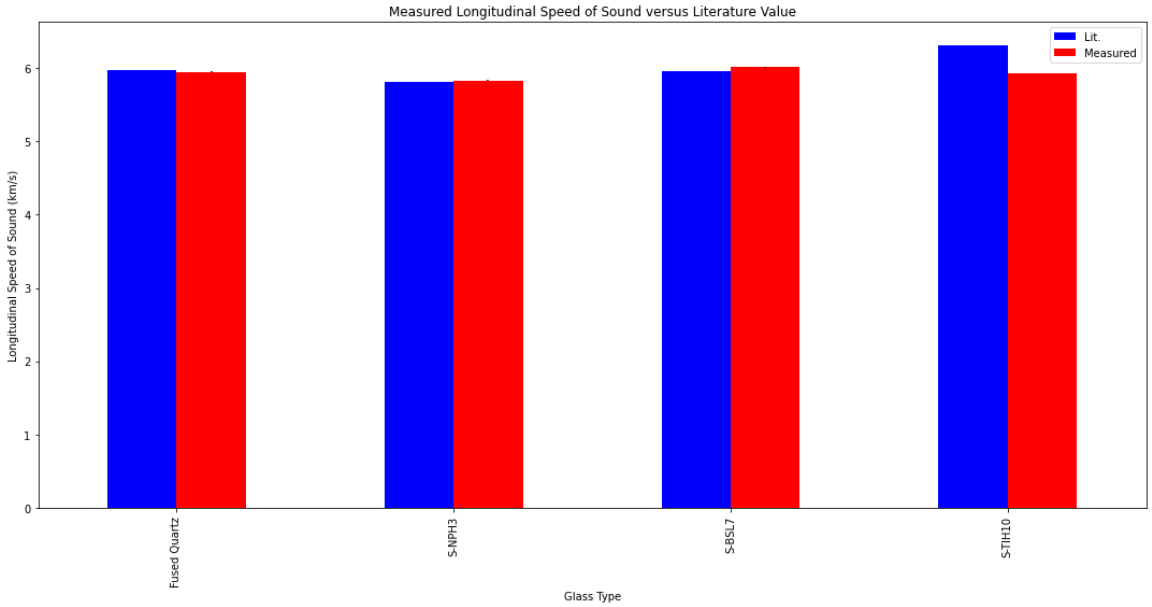

Figure 5.1: Comparison of reported values of the longitudinal speed of sounds compared to the measured values.

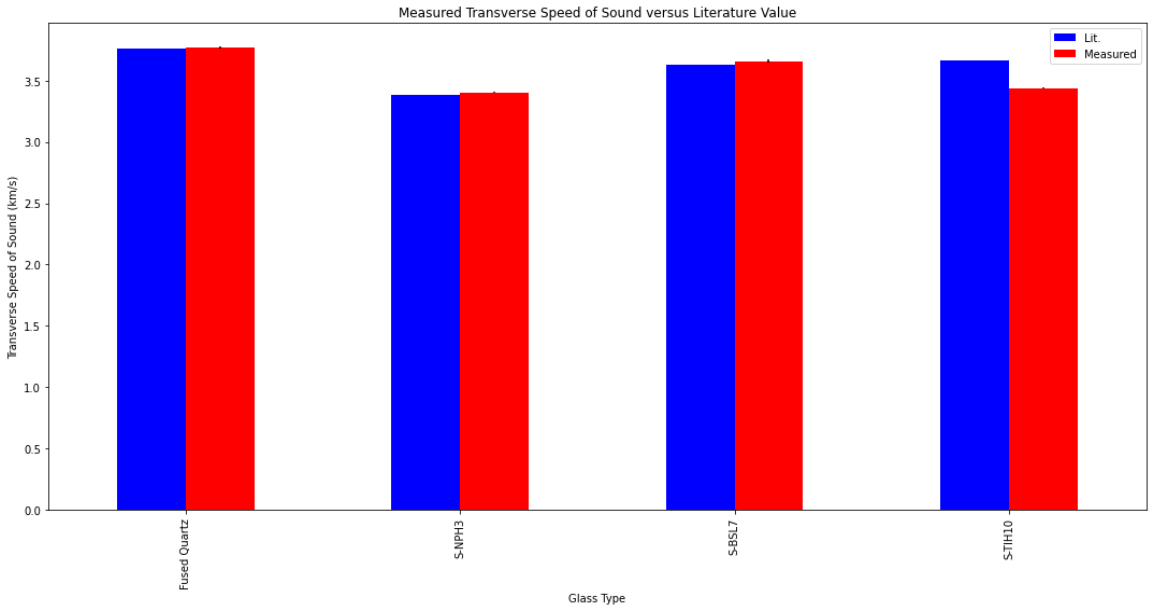

Figure 5.2: Comparison of reported values of the transverse speed of sounds compared to the measured values.

resolve this issue. Looking at the fused quartz data measured using the ellipsometer it is also higher than the accepted values at the selected wavelengths. The S-NPH3

data is the opposite, where the index of refraction is approximately 0.4 lower at the selected wavelengths compared to Table 3.1. The measured values of the longitudinal and transverse speed of sound are compared to the reported values in Figure 5.1 and Figure 5.2, respectively.

The reason for the refractive indices for S-BSL7 and S-TIH10 being higher than the reported values could be due to the boundary line between the light and dark area shown in Figure 3.1 was often not perfectly clear. This may be due to the contact fluid between the main prism and the sample which is fairly old or the use of too much contact fluid. Therefore some amount of judgment was taken to decide when the cross hairs were on the boundary line and would have resulted in the systematic error.

The disagreement between the fused quartz and the S-NPH3 refractive index data may be due to only having done one run using the ellipsometer. Unfortunately, our group did not have access to the machine and measurements were performed by a third party. A solution to this would be to do multiple runs at different locations on the sample and average the data. The comparison between the measured values reported in this work with literature values is presented in Figure 5.3.

The Sénarmont compensator results show the stress-optic coefficient for all four samples to be positive. The accuracy of the setup is poor due to the inability to obtain uniform stress throughout the sample. This causes the measured stress to be different compared to the actual stress in the sample where the laser beam is traveling. This results in the stress-optic coefficient being larger or smaller than the expected values given in Table 3.1. However, this setup allows for the determination of the sign of the stress-optic coefficient which is not provided by the acousto-optic setup. Figure 5.4 shows the comparison of the stress-optic coefficient measured by the Sénarmont compensator and the Dixon-Cohen methods to the reported literature values.

Comparing the stress-optic coefficients obtained using the Sénarmont compensator

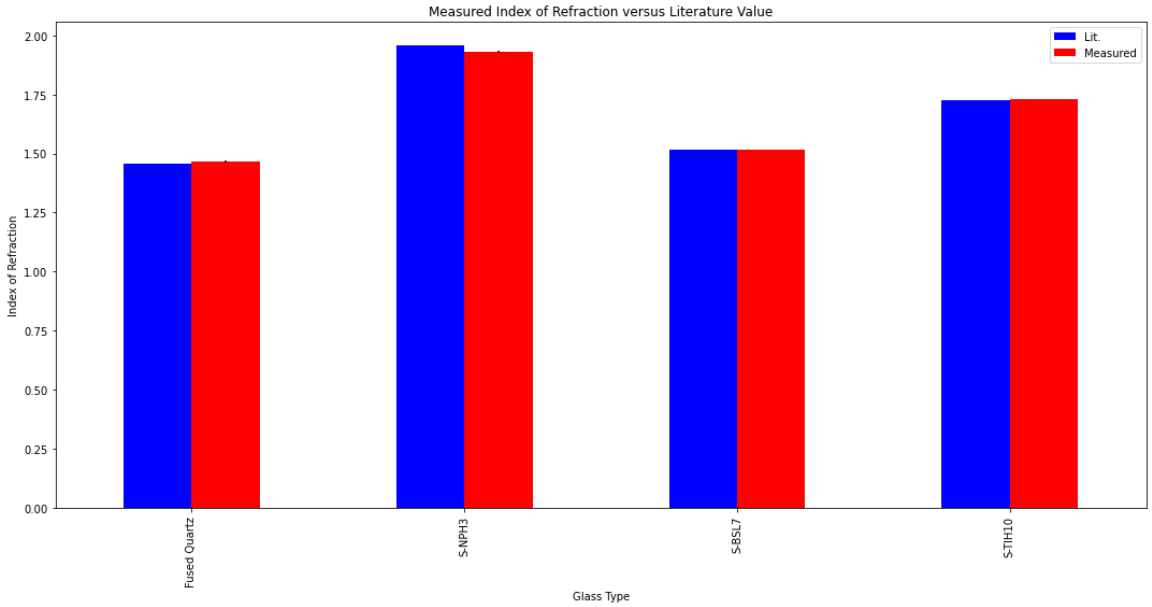

Figure 5.3: Comparison of reported values of the index of refraction to the measured values using the ellipsometer and the Abbe refractometer.

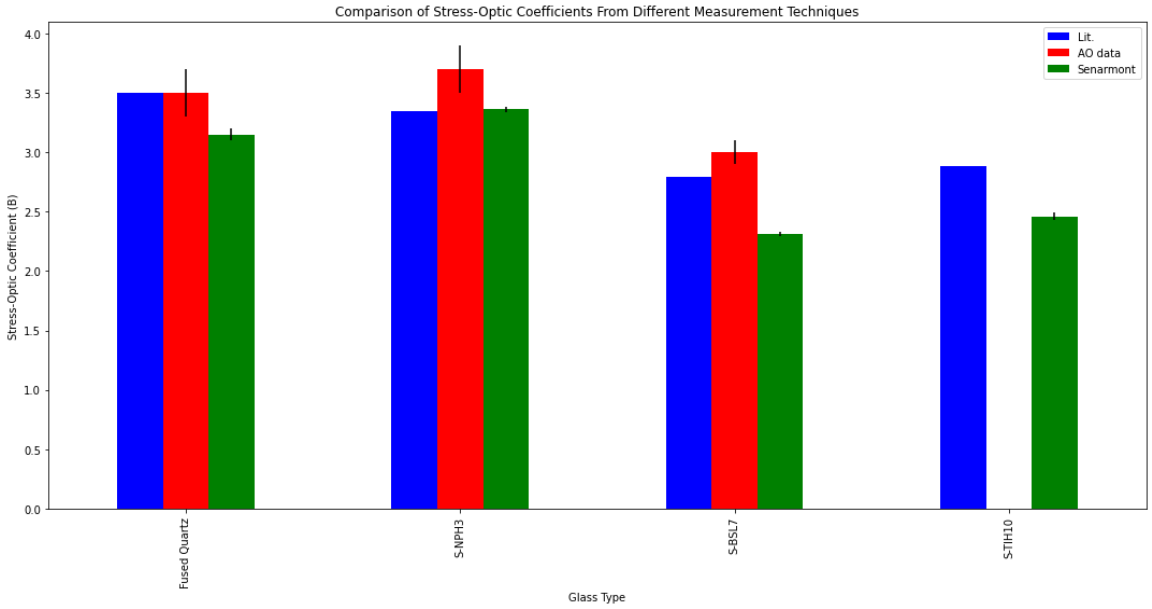

Figure 5.4: Comparison of reported values of stress-optic coefficients to the measured values by the Sénarmont compensator and the Dixon-Cohen method.

to that of the Dixon-Cohen method it can be seen for fused quartz that the AR coated fused quartz measured using the acousto-optic setup obtain a value equal within the uncertainty of that reported by Filon and Harris whereas the Sénarmont data is off

by more than 10% [40]. For this reason, the data obtained from the Sénarmont compensator can reliable indicate the sign of the stress-optic coefficient however fails to accurately determine the value.

The acousto-optic results for uncoated fused quartz were lower than the expected values measured by Dixon [39]. Part of this can be attributed to the lack of an AR coating resulting in a transmission loss of around 7%. However, the difference between the expected value and the measured value is approximately 18%. This additional discrepancy may be due to the size of the sample. The sample was slightly larger than the width of the acoustic beam so it is likely that the positioning of the sample on the reference piece did not sit directly over the acoustic wave and therefore resulted in some of the acoustic beam not being absorbed into the sample. This would result in a lower intensity of scattered light through the sample and also lead to a smaller back-reflected peak.

The AR-coated fused quartz results agree very well with the predicted value with a discrepancy of 1-2% for p_{11} and p_{12}. This is the same agreement obtained by Dixon and Cohen [30]. Comparing the peaks in the sample shown in Figure 4.11 for the AR-coated fused quartz to the uncoated fused quartz shown in Figure 4.9 it can be seen that more of the acoustic wave was transmitted into the sample resulting in higher beam intensities. As well, the back-reflected beam is much larger for the AR-coated fused quartz when compared to the uncoated fused quartz. This can be attributed to the fact that the AR-coated fused quartz was larger than the uncoated sample resulting in the full absorption of the acoustic wave.

Figure 4.13 and 4.14 show the acousto-optic results for S-NPH3 where a significant amount of the initial acoustic wave is transmitted into the sample. The back-reflected beam is quite small which may be due to acoustic losses at the boundary between the reference and the sample. This would result in the calculated values of p_{11} and p_{12} to be larger than the expected values based on Equation 2.41 where the back-reflected

intensity is in the denominator. When comparing the stress-optic coefficient found using the acousto-optic setup to that found in Table 3.1 this is the case. As well, the sample does not have an AR-coating which would result in the intensities measured in the sample to be lower than expected.

Figure 4.15 and 4.16 show the acousto-optic results for S-BSL7. In this case, the intial acoustic wave was not absorbed as well when compared to S-NPH3. This could be due to a poor bond formed between the sample and the reference causing the acoustic beam to reflect back into the reference rather than transmit into the sample. When comparing the calculated stress-optic coefficient to the data sheet it is again seen that the measured value is higher than the expected value.

The S-TIH10 sample could not be measured using the acousto-optic device due to issues with the sample breaking when being lapped. For this reason, the surface was not flat enough to form a good bond between the sample and the reference which resulted in no back-reflected peak being observed.

A solution to the poor bonding between the sample and the reference could be solved by lapping the surfaces to a smaller surface flatness than 1 um. This may result in better transmission of the acoustic beam into the sample making the results more accurate. As well, applying AR-coatings to all samples would decrease the reflectance loss and provide more accurate intensity measurements. In the case of S-NPH3 the reflectance loss is approximately 20% due to its high refractive index.

Chapter 6

Conclusion

The individual photoelastic tensor elements were able to be measured using the Dixon-Cohen method. The data presented for the AR-coated fused quartz sample shows that the acousto-optic setup can accurately measure the individual photoelastic tensor elements to within 1-2%. Issues with surface flatness and not having AR-coatings on the samples resulted in measured values being larger than the expected values based on the data sheets provided by Ohara.

Resolving the surface flatness issue would allow for a better bond between the sample and the reference resulting in more accurate results. This may be solved by lapping the surfaces to a smaller surface flatness than 1 um.

Applying AR-coatings to all samples would also increase the accuracy of the intensity measurements for all samples, especially those with a high refractive index.

As well, determining a way to uniformly stress the samples using the Sénarmont compensator would result in a second method to accurately determine the stress-optic coefficient and to validate the results obtained from the Dixon-Cohen method.

In conclusion, the Dixon-Cohen method has been shown to accurately determine the individual photoelastic tensor elements of AR-coated fused quartz, and in many cases provides reasonable values for the other glasses investigated. Future work needs to be done on surface flatness between the sample and the reference to provide better acoustic transmission into the sample. AR-coatings also need to be applied to all samples to be able to accurately calculate the photoelastic tensor elements.

Bibliography

[1] H. Scholze, *Glass: nature, structure, and properties*. Springer Science & Business Media, 2012.

[2] W. Vogel, *Glass chemistry*. Springer Science & Business Media, 2012.

[3] M. McArthur, "An in-situ investigation of solid electrolyte interphase formation of electrode materials for lithium-ion batteries using spectroscopic ellipsometry," Master's thesis, Dalhousie University, Halifax, Nova Scotia, Canada, 2011.

[4] W. H. Zachariasen, "The atomic arrangement in glass," *Journal of the American Chemical Society*, vol. 54, no. 10, pp. 3841–3851, 1932.

[5] A. Meshalkin and A. Kaplun, "Phase equilibria in the na2o–sio2 system," *Russian journal of inorganic chemistry*, vol. 48, no. 10, pp. 1567–1569, 2003.

[6] J. Galbraith, "Photoelastic properties of oxide and non-oxide glasses," 2014.

[7] A. K. Varshneya, *Fundamentals of inorganic glasses*. Elsevier, 2013.

[8] H. Bach and N. Neuroth, *The properties of optical glass*. Springer Science & Business Media, 1998.

[9] M. Guignard, L. Albrecht, and J. Zwanziger, "Zero-stress optic glass without lead," *Chemistry of materials*, vol. 19, no. 2, pp. 286–290, 2007.

[10] F. Pockels, "Über die änderung des optischen verhaltens verschiedener gläser durch elastische deformation," *Annalen der Physik*, vol. 312, no. 4, pp. 745–771, 1902.

[11] H. Mueller, "Theory of photoelasticity in amorphous solids," *Physics*, vol. 6, no. 6, pp. 179–184, 1935.

[12] S. Wemple and M. DiDomenico Jr, "Theory of the elasto-optic effect in non-metallic crystals," *Physical Review B*, vol. 1, no. 1, p. 193, 1970.

[13] S. Wemple and M. DiDomenico Jr, "Optical dispersion and the structure of solids," *Physical Review Letters*, vol. 23, no. 20, p. 1156, 1969.

[14] M. Cardona, D. Rönnow, and P. V. Santos, "Ellipsometric investigations of piezo-optical effects," *Thin Solid Films*, vol. 313, pp. 10–17, 1998.

[15] W. Kucharczyk, "Dispersion in the linear and second-order bond polarizabilities of alkali halides," *physica status solidi (b)*, vol. 182, no. 2, pp. 477–484, 1994.

[16] M. Tashiro, "The effects of the polarisation of constituent ions on the photoelastic birefringence of the glass," *J. Soc. Glass Technol.*, vol. 40, pp. 353T–362T, 1956.

[17] A. Rabukhin and G. Belousova, "Photoelastic constants of bismuth-containing gallate glasses," *Glass and ceramics*, vol. 49, no. 10, pp. 458–462, 1992.

[18] K. MATUSITA, R. YOKOTA, T. KIMIJIMA, T. KOMATSU, and C. IHARA, "Compositional trends in photoelastic constants of borate glasses," *Journal of the American Ceramic Society*, vol. 67, no. 4, pp. 261–265, 1984.

[19] K. MATUSITA, C. IHARA, T. KOMATSU, and R. YOKOTA, "Photoelastic effects in silicate glasses," *Journal of the American Ceramic Society*, vol. 67, no. 10, pp. 700–704, 1984.

[20] K. MATUSITA, C. IHARA, T. KOMATSU, and R. YOKOTA, "Photoelastic effects in phosphate glasses," *Journal of the American Ceramic Society*, vol. 68, no. 7, pp. 389–391, 1985.

[21] A. Rabukhin, "Photoelastic constants of germanate glasses containing lead and bismuth oxides," *Glass and ceramics*, vol. 51, no. 11-12, pp. 353–359, 1994.

[22] N. K. Sinha, "Normalised dispersion of birefringence of quartz and stress optical coefficient of fused silica and plate glass," 1978.

[23] A. A. Manenkov and A. I. Ritus, "Determination of the elastic and elasto-optic constants and extinction coefficients of the laser glasses lgs-247-2, lgs-250-3, lgs-i, and kgss-1621 by the brillouin scattering technique," *Soviet Journal of Quantum Electronics*, vol. 8, no. 1, p. 78, 1978.

[24] P. Benassi, V. Mazzacurati, G. Ruocco, and G. Signorelli, "Elasto-optic constants in silicate glasses: Experiment and theory," *Physical Review B*, vol. 48, no. 9, p. 5987, 1993.

[25] X. Roselló-Mechó, M. Delgado-Pinar, A. Díez, and M. Andrés, "Measurement of pockels' coefficients and demonstration of the anisotropy of the elasto-optic effect in optical fibers under axial strain," *Optics letters*, vol. 41, no. 13, pp. 2934–2937, 2016.

[26] J. Galbraith, L. Chapman, J. Zwanziger, M. Aldridge, and J. Kieffer, "Elasto-optic coefficients of borate, phosphate, and silicate glasses: determination by brillouin spectroscopy," *The Journal of Physical Chemistry C*, vol. 120, no. 38, pp. 21802–21810, 2016.

[27] A. Korpel, "Acousto-optics—a review of fundamentals," *Proceedings of the IEEE*, vol. 69, no. 1, pp. 48–53, 1981.

[28] T. S. Narasimhamurty, *Photoelastic and electro-optic properties of crystals*. Springer Science & Business Media, 2012.

[29] D. J. Griffiths, *Introduction to electrodynamics third edition*. Prentice Hall, Inc., 1999.

[30] R. Dixon and M. Cohen, "A new technique for measuring magnitudes of photoelastic tensors and its application to lithium niobate," *Applied Physics Letters*, vol. 8, no. 8, pp. 205–207, 1966.

[31] L. Brillouin, "Diffusion de la lumière et des rayons x par un corps transparent homogène-influence de l'agitation thermique," in *Annales de physique*, vol. 9, pp. 88–122, EDP Sciences, 1922.

[32] Y. Aoki, K. Tajima, and I. Mito, "Input power limits of single-mode optical fibers due to stimulated brillouin scattering in optical communication systems," *Journal of Lightwave Technology*, vol. 6, no. 5, pp. 710–719, 1988.

[33] A. Kobyakov, M. Sauer, and D. Chowdhury, "Stimulated brillouin scattering in optical fibers," *Advances in optics and photonics*, vol. 2, no. 1, pp. 1–59, 2010.

[34] E. Ippen, "Low-power quasi-cw raman oscillator," *Applied Physics Letters*, vol. 16, no. 8, pp. 303–305, 1970.

[35] A. Melloni, M. Frasca, A. Garavaglia, A. Tonini, and M. Martinelli, "Direct measurement of electrostriction in optical fibers," *Optics letters*, vol. 23, no. 9, pp. 691–693, 1998.

[36] R. Chiao, C. Townes, and B. Stoicheff, "Stimulated brillouin scattering and coherent generation of intense hypersonic waves," *Physical Review Letters*, vol. 12, no. 21, p. 592, 1964.

[37] F. L. Pedrotti, L. M. Pedrotti, and L. S. Pedrotti, *Introduction to optics*. Cambridge University Press, 2017.

[38] R. C. Jones, "A new calculus for the treatment of optical systems. iv.," *Josa*, vol. 32, no. 8, pp. 486–493, 1942.

[39] R. Dixon, "Photoelastic properties of selected materials and their relevance for applications to acoustic light modulators and scanners," *Journal of Applied Physics*, vol. 38, no. 13, pp. 5149–5153, 1967.

[40] L. N. G. Filon and F. Harris, "The photo-elastic dispersion of vitreous silica," *Proceedings of the Royal Society of London. Series A, Containing Papers of a Mathematical and Physical Character*, vol. 130, no. 813, pp. 410–431, 1931.